Nanoscale

ROYAL SOCIETY OF CHEMISTRY

PAPER

View Article Online
View Journal | View Issue

Check for updates

Cite this: *Nanoscale*, 2026, **18**, 8278

Enhanced absorption and fluorescence quenching methods for the quantitative analysis of Cr(VI) ions using avocado seed-derived carbon quantum dots as pseudo-derivatising reagents

Amahle Mkhize,[a] Xolani Nocanda,[b] Irvin Noel Booysen *[a] and Allen Mambanda *[a]

Received 2nd October 2025,
Accepted 9th February 2026

DOI: 10.1039/d5nr04174k

rsc.li/nanoscale

Water pollution by chromate wastes is pervasive and requires selective and sensitive low-cost methods for quantification. Herein, we report the enhanced absorption and fluorescence methods for the quantitative analysis of chromium(VI) ions using avocado seed-derived carbon quantum dots as pseudo-derivatising reagents. Sulfur- and nitrogen-doped green carbon dots (S, N-CDs) were hydrothermally synthesised from an avocado seed powder extract and were characterised by various techniques. The S, N-CDs selectively detect Cr(VI) by enhanced absorption at Cr(VI)'s charge transfer band at 375 nm and fluorescence quenching at 420 nm. Both modes were used for nanomolar detection of the latter in the presence of other metal ions at a 100-fold higher concentration. Mn(VII) ions interfere with the Cr(VI) responses. At pH 9, the enhanced absorption method showed a linear correlation with the [Cr(VI)] range of 0.5–1500 ppb, yielding estimated LOD and LOQ values of 0.14 ppb and 0.49 ppb, respectively. The quenching of the S, N-CDs fluorescence linearly varied with the [Cr(VI)] in the 20–1500 ppb concentration range, giving estimated LOD and LOQ of 5.9 and 25 ppb. Both methods showed good recovery (89–99%) for ppb levels of Cr(VI) spiked in river water samples. They could detect Cr(VI) in contaminated laboratory waste (positive control) with good comparability and accuracy compared to the ICP-OES result. Thus, these two spectrochemical methods derived from avocado seeds as pseudo-sensing reagents can be used for the quantitative detection of Cr(VI) ions at ppb levels, surpassing conventional calorimetric detection of Cr(VI) after a derivatising step.

Introduction

The pollution of water resources with heavy metal ions is a global threat to the ecological balance of microorganisms and microflora.[1] Urban water resources and aquatic ecosystems are more susceptible to heavy metal pollution from human-related activities, including mining, mineral processing, effluent spillage and discharges, metal application and handling industries, and leaching from landfills that receive metal-contaminated solid waste. One of the classes of heavy metal compounds/complexes that commonly contaminates water resources are the chromates (Cr(VI) species). Chromates are non-essential, highly water-soluble, and potent oxidising agents.[2,3] They damage cells and impair the function of proteins. Chronic exposure to chromates leads to carcinogenic and mutagenic effects in animals and humans.[4]

In South Africa, the demand for clean water has surpassed supply, particularly in urban areas. This has led to limited access characterised by a scarcity of clean and potable water. There are growing concerns that a significant amount of effluent and emissions laden with heavy metals are released into the urban environment and ultimately into the aquatic environments, which often serve as sources of freshwater for domestic and industrial purposes. South Africa is endowed with ferrochrome ($FeCrO_4$) reserves.[5–9] However, the mining and mineral processing of $FeCrO_4$ present an environmental pollution challenge, especially in the vicinity of water bodies and courses. Seasonal survey studies of Cr(VI) in surface and underground water samples collected in South Africa's Bushveld Mineral Complex (Rustenburg area) revealed widespread Cr(VI) contamination of groundwaters at some sites. However, the concentration levels in surface waters were generally low.[5–9] Besides the ferrochrome value-added processes, other sources of concern regarding chromate pollution include

---

[a] School of Chemistry and Physics, University of KwaZulu-Natal, Private Bag X01, Scottsville 3209, Pietermaritzburg, South Africa. E-mail: mambanda@ukzn.ac.za, Booyseni@ukzn.ac.za
[b] Council for Scientific and Industrial Research, Water Centre, Brummeria, Pretoria, 0001, South Africa

chromium plating, leather tanning, paints, dyes, explosives, ceramics, and paper manufacturing.

Given the potential contamination of surface and groundwater sources by chromates, the continued development of more sensitive, cost-effective, and sustainable analytical methods for the regular monitoring of Cr(VI) in air, soil, sediment, and water samples is necessary. Furthermore, the contamination and prevalence of Cr(VI) ions in urban trade waste and the hydrological basin and impoundments are pervasive, necessitating innovative, cost-effective, and reliable analytical methods for regular monitoring of these toxic ions. However, the current quantitative methods for Cr(VI) analysis, including atomic absorption spectroscopy (AAS), inductively coupled plasma-optical emission spectroscopy (ICP-OES), and inductively coupled plasma mass spectroscopy (ICP-MS), are expensive to acquire and limited to established analytical laboratories. In contrast, optical-based methods (calorimetric absorption or molecular fluorescence) are relatively lower-cost, easier to use, and suited for real-time detection, making them sensitive enough to detect and quantify ultra-trace amounts of Cr(VI) in water resources.[10–14] Moreover, USEPA set the calorimetric method based on the pre-derivatizing of Cr(VI) ions with 1,5-diphenyl carbazide as the reference method (EPA Ref No. 7196A, 1992) for the detection and quantitative analysis of Cr(VI) in water in the USA.[15,16] However, the detection limits are typically in the sub-ppm range with a narrower linear range of 0.5–50 mg L^{-1} (ppm). Similar absorption methods for Cr (VI), including the direct absorption method, have been reported in the literature.[12,16] However, poor sensitivity and linear concentration ranges, as alluded to in the USEPA method, limit their versatility in ultra-trace analysis of Cr(VI).

The development of more sensitive optical methods for Cr (VI) and other metal ions,[17–21] which utilise carbon nanomaterials, such as carbon quantum dots (CQDs), as fluorometric reagents, has taken centre stage. CDs are quasi-spherical carbon nanomaterials (with a size typically ≤ 10 nm) containing sub-nanodomains comprising graphitic (sp^2 carbons) core domains and defect regions characterised by sp^3-hybridised carbons. They are endowed with different functional groups containing heteroatoms. These functional groups are typically located on the surfaces of the dots or at the edges of the graphitic planes of the carbon dots. CDs are highly water-soluble. They influence interactions with specific analytes, thereby affecting selectivity and sensitivity in the detection of these analytes.[22–26] CDs emit an intense wavelength-dependent characteristic radiation when excited by ultraviolet-visible radiation. The emission of these fluorescence carbon dots (FCDs) depends on the size of the CDs and dopants (N, S, P, B, *etc.*), excitation wavelength, and other factors. Due to the tunable properties of CDs, they have found widespread use in biomedical applications (cell imaging, drug delivery, and phototherapy), photocatalysis, electrocatalysis, and, importantly, as fluorometric sensing probes for heavy metals and organic pollutants.[19,27–29]

It is well known that the quasi-binding of the heavy metal ions, such as Cr(VI) or small organics, onto the surface functional groups of the FCDs quenches (turns off) their emission. The quenching is correlated with the metal ion concentration. Hence, it has been used for the quantitative determination of metal ions *via* the Stern–Volmer linear calibration protocol. For example, quantitative fluorescence quenching methods for Cr(VI) have been reported with improved specificity and sensitivity.[30,31] FCDs have also been used as 'turn on' sensing reagents for the fluorometric detection of metals and the quantitative analysis of Cr(VI), as well as subsequently ascorbic acid.[32]

The quantitative determination of Cr(VI) by the fluorescence quenching methods has shifted towards using sustainably derived FCDs. The production of carbon nanomaterials incorporates the principles of green chemistry or upcycling of plant- and animal-based materials (biomass). Various biomass sources have been used to afford surface-passivated FCDs for detecting metal ions such as Cr(VI),[33] Fe(III),[34] and Hg(II).[35] Utilising non-edible components of fruits, such as *Persea Americana Mill* (Avocado) seeds, is a sustainable approach to waste utilisation, potentially yielding high-value materials or spin-off technologies and innovations. Avocado seeds are a degradable biomass; they are inedible to humans and animals, and hence, they are discarded into the environment, increasing the amount of organic matter in the aquatic environment and the demand for dissolved oxygen. The seeds contain several bioactive compounds, such as carbohydrates, hydroxylated minerals, carbonyl lipids, and a diverse range of phytochemicals (bio-reductants) such as tannins, polyphenols, polyflavonoids, *etc*. These natural compounds can be utilised in the bottom-up synthesis of CDs as sustainable analytical reagents for sensing applications.[36–38]

While the use of FCDs as fluorescence quenching reagents for the quantitative analysis of metal ions is extensively studied,[32,39–46] not much has been reported on them as reagents for sensing metal ions in the enhanced absorption mode. Only recently have CD-based absorptive detection methods been reported for quantitative analysis of Cr(VI),[47] Cu(II),[48,49] Pb(II),[34] Ag(I),[50] and Co(II),[48,51] respectively. These studies do not sufficiently demonstrate the origin of the enhanced absorption and utilise CDs synthesised from non-sustainable and expensive synthetic chemicals as carbon sources, compared to the upcycling of avocado seed (a plant waste) that has been utilised in this study. Pizzoferrato and co-workers[47] used N-CDs derived from the oxidative etching of synthetic fullerene (C_{60}), stabilised in water/THF basic solutions, for the calorimetric detection and quantitative analysis of Cr(VI). The calibration data exhibited a linear range with 1–100 μM and a LOD value of 300 nM (15.6 ppb). A dual-mode UV-Visible and fluorescence quenching method for the quantitative analysis of Pb(II) developed by Yarur *et al.* exhibited a linear range of 1–961 nM (0.05–50 μM) for the absorption mode and a detection limit of 37.1 nM (7.69 ppb) for Pb (II).[34] In a similar approach, the dual mode analysis of Co(II) was performed by both methods with a linear range of 0–200 μM, and the LODs were 100.2 nM and 750 nM, respectively.

In this work, we synthesised sulfur- and nitrogen-doped fluorescent carbon dots (S, N-FCDs) using a one-pot hydrothermal synthesis method derived from avocado seeds, making these carbon nanomaterials eco-friendly as advocated in the UN's Sustainable Development Goal 17. In the newly developed UV-Visible enhanced absorption and fluorescence quenching methods, the S, N-FCDs were utilised as pseudo-derivatising reagents for detecting and quantitatively analysing trace levels of Cr(VI) (with sub-ppb LODs). This allowed us to compare the analytical performances of the two new methods towards the quantitative analysis of Cr(VI). Furthermore, their accuracy in studying Cr(VI) ions in spiked river water and control positive samples was cross-validated with the results of the ICP-OES.

2. Materials, methods, and Instrumentation

2.1 Materials and reagents

The semi-ripe "Hass" avocado, *P. Americana's* fruit, was purchased from a retail grocery in Scottsville, Pietermaritzburg, KwaZulu-Natal, South Africa, and stored in a refrigerator until it was cut open to remove the seeds. All chemicals, solvents, and consumables were purchased from Merck-Sigma Aldrich and used without further purification. Analytical grade reagents such as thiosemicarbazide, NaOH, $K_2Cr_2O_7$, NaCl, $MgSO_4$, $CuSO_4$, H_2SO_4, $PbCl_2$, KCl, $Al(NO_3)_3 \cdot 9H_2O$, $HgCl_2$, $CrCl_3 \cdot 6H_2O$ and $KMnO_4$ were used; ultrapure water was utilized in all general experiments.

2.2 Synthetic procedures

2.2.1 Hydrothermal synthesis of sulfur, nitrogen-doped carbon dots (S, N-CDs) from the avocado seed powder (ASP). The preparation of the avocado seed powder (ASP) is described in the SI (SI S1). A mass of 5.000 g of ASP was accurately weighed and dispersed in 15 mL of a 1 : 4 EtOH : H_2O solution and refluxed for 12 h at 60 °C. Afterwards, the solution was subjected to sequential centrifugation and sonication at 6000 rpm for 5 and 10 minutes, respectively. The supernatants containing the avocado seed extract were combined, and the pellets were further suspended in 2 mL of solvent. The mixture was then sonicated and centrifuged for 5 minutes. The process was repeated thrice, and the combined extracts' volume was adjusted to 25.00 mL. The extract was labeled as 20% (w/v) ASP extract and was used to synthesise the S, N-CDs. To 10.00 mL of the ASP extract, 40.00 mg of thiosemicarbazide was added (as a doping source of sulfur and nitrogen (S, N) atoms). The mixture was preheated for 2 h at 60 °C and cooled, and the pH was adjusted to 2 using 9 M H_2SO_4. The mixture was transferred into a 50 mL Teflon-lined hydrothermal steel autoclave microreactor. The reactor body was heated in an oven at 180 °C for 6 h. A dark lavender-orange crude solution and a settleable brownish precipitate or colloids at the base were obtained. The supernatant was transferred; colloids were washed twice with the 2 × 2.0 mL 1 : 4 EtOH : H_2O aliquots, and the washes were combined with the supernatant. The combined supernatants were purified through three sequential ultra-centrifugation, filtration, and wash steps. Centrifugation was performed at 12 000 rpm for 15 minutes, followed by micro-filtration through 0.22 μm Millipore filters. The purified N-FCDs were yellowish under normal light and remained stable as a 1 : 4 EtOH : H_2O homogeneous solution.

To remove the solvent (water/EtOH), an aliquot of the S, N-FCD solution was freeze-dried six times in liquid nitrogen at 30-minute intervals, aided by a high vacuum pumping system. At each step, a few drops of warm water were added to induce sublimation, leaving behind a dark orange-brown paste. The residue was scraped off and dried over a flowing stream of nitrogen in the fume hood for a week. Afterwards, it was ground in a pestle and mortar to obtain an orange-brown powder of the S, N-FCDs. The synthetic steps are illustrated in Scheme 1. Thereafter, the powder was examined using TEM, SEM-EDX, FT-IR, PXRD, and XPS equipment, and a zeta potential analyser.

2.3 Instrumentation for the characterisation of the S, N-CDs

A Waring blender was used to grind the avocado seed into powder. A Lasec (Compact MDL Z206A, 6000 rpm) and a centrifuge PLC series (12 000 rpm) were used for sequential sedimentation to attain S, N-CDs of a reduced size range and better optical purity. The S, N-CD powder was drop-cast onto a gold-coated copper grid, and the size and shape of the S, N-CDs were visualised and measured using a JEOL JEM-1400 transmission electron microscope (TEM) with an 80 kV electron beam source. The sizes of the S, N-CDs were measured using ImageJ software. The N, S-CD ink was also spotted onto a gold-coated copper grid, and the surface morphology, dispersibility, as well as elemental composition were measured and visualized on a Quorum Q150R ES (SEM-EDX) scanning electron microscope-energy dispersive X-ray spectrometer. A Nano Series Zetasizer ZS (Malvern Panalytical) with onboard Zetasizer software was used to measure the zeta potential (ζ) of the S, N-CDs before and after mixing Cr(VI). A Nano Flash fluorescence spectrometer (Photon Technology International (PTI)) with onboard Felix32 software was used to record and evaluate the photoluminescence of the S, N-CDs. A Rigaku Miniflex 600 diffractometer was used to acquire the powder X-ray diffraction spectrum of the S, N-CDs. The survey and deconvoluted X-ray photon spectra (XPS) were recorded and evaluated on the Thermo ESCALabXi (X-ray energy = 1486.7 eV, power = 300 W, spot size = 900 μm, 10^{-8} mBar) at the National Metrology Institute of South Africa (NMISA). The frequency vibrational band and the functional groups of the S, N-CDs were measured on the Bruker Alpha 1 Fourier transform infrared (FTIR) spectrometer as a powder spread on an attenuated total reflectance (ATR) platinum Diamond 1 accessory. Ultraviolet-visible (UV-Vis) absorption spectra were recorded on an Agilent Cary 60 spectrophotometer in the 200–800 nm range. Cr in spiked samples was measured on an inductively coupled plasma-optical emission (simultaneous) spectrometer (ICP-OES) (ICPE-9820 Series, Shimadzu).

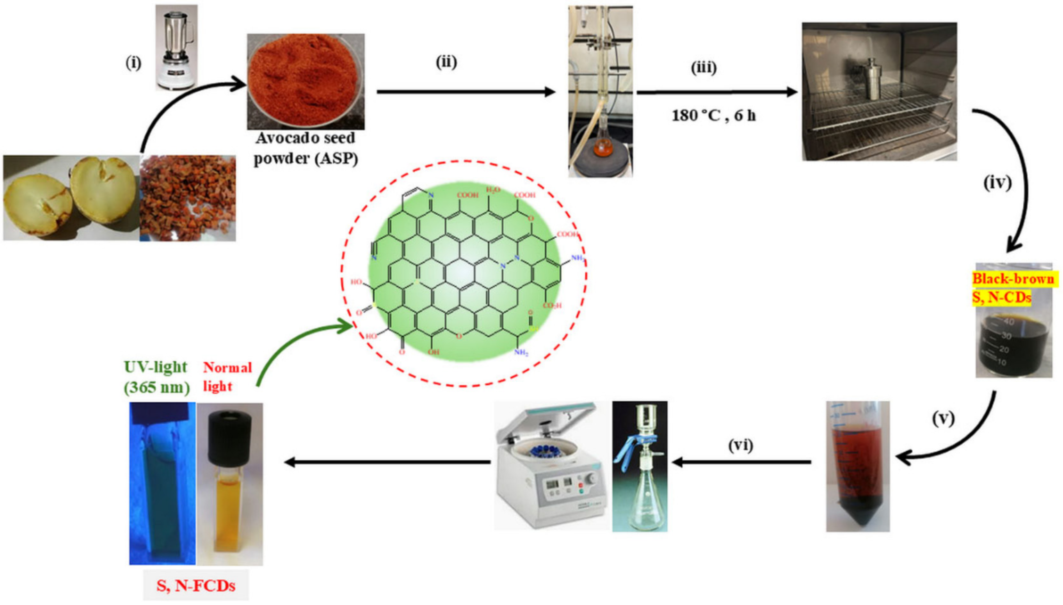

Scheme 1 The hydrothermal synthesis of S, N-CDs from avocado seed powder (ASP) for 6 h at 180 °C, where (i) shows the pulverization of diced avocado seeds into powder and drying for 6 h at 70 °C; (ii) shows the ASP extraction with 1 : 4 EtOH/water at reflux for 12 h followed by S, N-atom doping with thiosemicarbazide; (iii) shows the hydrothermal synthesis of CDs from an ASP extract (placed in an oven-heated Teflon-lined micro-steel reactor) for 6 h at 180 °C. The pH was adjusted to *ca.* 2 (9 M H_2SO_4); (iv) shows the cooling of the as-synthesised mixture to obtain an air-stable and concentrated brown-black S, N-CD solution, and (v) & (vi) show the sequential and repeated (N = 5) ultracentrifugation-sub-micromembrane filtration (0.22 μm) steps.

2.4 Application of S, N-CDs for quantitatively determining Cr(VI) ions

2.4.1 Linear calibration by the host–guest surface interactive absorption (HGSIA) and fluorescence (FLUOR) quenching methods. Incremental aliquots of 100 mg L^{-1} (for the higher concentration range) or 10.00 mg L^{-1} (for the lower concentration range) of $Cr_2O_7^{2-}$ and a fixed volume of 0.1 M NH_3/NH_4^+ (pH 9) were added to 2.00 mL of the S, N-FCDs to attain final Cr(VI) concentrations in the 0.5–1500 ppb range. The absorption spectra of the host–guest surface interactive absorption (HGSIA) of the S, N-CDs, and the Cr(VI) standards in S, N-CDs were recorded and presented as overlays. The normalised absorbance data at 375 nm were plotted against the dichromate concentration ($[Cr_2O_7^{2-}]$) to obtain a linear calibration curve equation, from which the slope (calibration sensitivity) and R^2 value were recorded.

Similarly, the quenched fluorescence (after excitation at 310 nm) of the prepared Cr(VI) in S, N-FCD calibration standards (used in the HGSIA method and with final Cr(VI) concentrations in the 20–1500 ppb range) was measured at 420 nm. The normalised quenched fluorescence was plotted against $[Cr_2O_7^{2-}]$ to obtain a linear calibration curve equation from which calibration parameters (calibration sensitivity, R^2 coefficient, the limit of quantification (LOQ), and limit of detection (LOD)) were deduced.

Replicated measurements (N = 15) of the absorption or emission of the S, N-CDs at 375 nm (the reagent blank) of S, N-CDs, and applying the data to eqn (S2) and (S3) yielded the estimated LOQ and LOD values for each method from the formulae LOD/LOQ = $\{3\sigma/(10)\}/k$, where k = slope of the calibration curve and σ is the standard deviation of the blank.

2.5 Real water sample analysis

Contamination of soils and water by chromates (Cr) is often a worrying environmental problem (Cr). The accuracy (as % Cr (VI) recovery) of the HGSIA or quenched FLUOR method for Cr (VI) measurements was evaluated at two low concentration levels in spiked Msunduzi River water, which had been collected from the Pietermaritzburg area (latitude: −27°37′8.39″ and longitude: 30°40′21.59″). The water sample was centrifuged at 12 000 rpm to remove large particles and filtered with a 0.22 μm membrane filter. The water was used to prepare 8.3 mg L^{-1} N, S CDs. Two aliquots, 1.98 and 1.80 mL of the CDs (in river water), were spiked with 20 μL and 200 μL 10 mg L^{-1} Cr(VI) in N, S-CD standards, respectively. The final Cr(VI) concentrations in the two spiked river water samples were 20 ppb and 200 ppb, respectively. The enhanced absorbances or FLUOR quenching of the unspiked (N, S-CDs in water), 20 ppb and 200 ppb Cr(VI) in S, N-CDs/river water samples were recorded at 375 nm and 420 nm, respectively. No absorbance (375 nm) or FLUOR quenching (420 nm) changes were recorded for the water on CDs in the River water. The % recovery of Cr(VI) at the two spiked levels by both methods was deduced from the calibration equation.

Procedures to estimate the quantum yield of the fluorescence of the S, N-CDs, to verify the enhanced absorption (host–guest enhanced absorption interactions – HGSIA) of Cr(VI) in the S, N-CD solution, confirm the selectivity over other potential interferences for both the HGSIA and fluorescence (FLOUR) methods; the effect of pH on the fluorescence of the CDs, their photostability, ionic interferences, and photo-oxidation are outlined in the SI (S2–S7). The procedures for validating the precision of Cr(VI) detection and accuracy (as % recoveries) in spiked samples and in a positive control (Cr(VI) contaminated) sample by both methods *via* standard addition, and cross-validating the analytical performances of both methods by ICP-OES are given in the SI S8–S10.

3. Results and discussion

3.1 Synthesis and characterisation of S, N-CDs

In this work, hydrothermal heating of an avocado seed powder extract (20 w/v%) and 40.0 mg (2 w/w%) thiosemicarbazide (an N, S atom-dopant) under acidic conditions, in a 1 : 4 EtOH/H_2O mixture, resulted in a colored solution of the S, N-CD colloids. The colloids emitted a dull green fluorescence under irradiation with a 365 nm lamp. The yellow solution is obtained through sequential ultracentrifugation and microfiltration (using a 0.22 µm nitrocellulose filter) steps. It is a water-soluble and stable nanocolloid of the S, N-CDs. Freeze-drying of the S, N-CD colloids through sequential immersion in liquid nitrogen afforded a light brown powder, which was fully characterised by various surface characterisation techniques.

The size distribution and particle sizes of the S, N-CDs were analysed by TEM, and the obtained micrographs are shown in Fig. 1A–C. The synthesized S, N-CDs are monodisperse and quasi-spherical clusters within the particle size range of 8.5–18 nm Fig. 1B. Under the synthetic reaction conditions (elevated temperatures and pressure and condensed state), in a polar solvent mixture (1 : 4 EtOH/H_2O), nonspecific thermal reactions that include carbon chain growth, cross-linking, dehydration, condensation, rearrangement and ring fusion of the compounds in the aqueous extract of the avocado seed (the carbon source) and the minute amounts of thiosemicarbazide (the N, S dopant) occurred. These ultimately formed nanometric core graphene domains (the microcrystalline region) that grew into the quasi-spherical S, N-doped carbon dots.

The surface morphology of the N, S-CDs that were synthesised under oxidising acidic conditions is shown in Fig. 1D and E. The CDs appear as interwoven aggregates of randomly folded nanosheets and granular carbon rods, presenting a rough surface topology with random crevices. This surface morphology increases the effective surface area of the S, N-CDs, allowing them to react more efficiently with target analytes. The discrete graphitic carbon nanorods are randomly oriented and stacked onto the surface of folded graphene-like nanosheets. Some carbon rods are crystalline, and their orientation exposes crevices and nano-void pores. The new orthogonal nanosheets sprout from the body of the nanorods, as shown in Fig. 1D. The EDX spectrum of the S, N-CDs shown in Fig. 1F confirms the presence of C (28.3%), O (31%), S (14.2%), N (8.74%), and K (17.7%). The addition of thiosemicarbazide as a doping agent increased the percentage composition of S and N atoms. At the same time, the high %K (potassium) content detected in the EDX spectrum of the S, N-CDs is correlated with its natural content in the avocado seed that was used as a carbon source, since no potassium salt was used in the synthesis of the S, N-CDs. The SEM-EDX elemental mapping diagrams of the S, N-CDs shown in Fig. S1 depict the elemental dispersion of the atoms found in the CDs. The

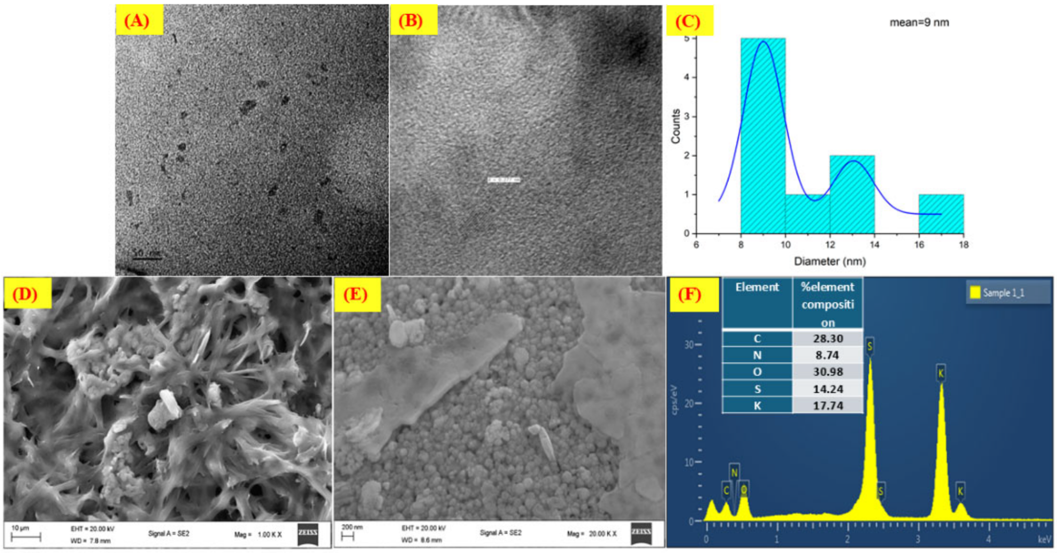

Element	%element composition
C	28.30
N	8.74
O	30.98
S	14.24
K	17.74

Fig. 1 (A) TEM images of the avocado seed powder-derived S, N-CDs; (B) HR-TEM image of the obtained S, N-CDs; (C) Histogram of the size distribution of the S, N-CDs; (D and E) SEM images of the S, N-CDs; (E) SEM image of graphitic nanosheets of the S, N-CDs, and (F) SEM-EDX of S, N-CDs showing the elemental composition.

intensity of elemental mapping for the S, N-CDs decreases in the order C (28.3%) > O (31%) > S (14.2%) > N (8.74%), corroborating that these heteroatom functional groups decorate the paper-like graphitic nanosheets and nano-spherical S, N-CDs on their surfaces. The electrostatic surface potential of the S, N-CDs shows a large negative value, as evidenced by a negative zeta potential (ζ) of −5.66 (±0.07) mV (Fig. S2B). This is due to defects in the graphitic material that are passivated by negatively charged functional groups, such as hydroxyl, thiol, and amide groups. The SEM image (Fig. S2A) of the S, N-FCDs mixed with 100 ppb Cr(VI) ions (the target ion for detection) exhibits a smoother, dotted pattern with graphitic, clustered, and spherical nanoparticles. The observed surface morphology changes are likely related to the declustering of the CDs due to surface non-covalent interactions. These interactions can result in a more diffuse electron beam, leading to a faded image that appears as a smooth surface. Thus, the quenching of fluorescence, as seen in Fig. S2A, is evidence of surface passivating interactions between the synthesised S, N-CDs and Cr (VI), which can be used to detect trace-level amounts of the latter. Moreover, the (ζ) value increases from −5.66 (± 0.07) mV (for the S, N-CDs) to +4.22 (± 0.05) mV when the S, N-CDs are mixed with the high oxidation state and electropositive Cr(VI) ions (Fig. S2C).

The PXRD analysis was used to elucidate and probe the phase and crystallinity of the S, N-FCD powder. As shown in Fig. 2A, the carbon nanomaterials feature several sharp peaks superimposed on broader peaks with the diffraction 2θ angle range of 18–45°. The sharp peaks indicate that the S, N-FCDs have some phase domains with a degree of crystallinity, while the broader peaks represent amorphous carbon domains. For example, a sharp diffraction peak at $2\theta = 25°$ is typical of reflection by a (002) graphitic mirror plane.[52] Other sharp peaks occur at $2\theta = 40.2°$ (100) and 46° (102), corresponding to the in-plane diffraction of the graphitic core mirror planes of the S, N-FCDs. The PXRD data indicate that the S, N-FCDs are predominantly amorphous.

FT-IR was used to probe the different functional groups on the surface of the avocado seed powder extract, and the S, N-CDs, and the recorded overlay spectra are presented in Fig. 2G. The former (avocado seed powder) does not show as many discrete and intense vibrational peaks as the S, N-CDs. This could be due to the dilution effect in the avocado seed water/EtOH extract. On the other hand, the S, N-CD FT-IR spectrum exhibits a diverse range of surface functional groups, characterised by medium to intense vibrational peaks. Prominent peaks were observed at the following vibrational frequencies, ν, 3500–3600 cm^{-1} ν(O–H, w/br, unresolved shoulder); 3315 cm^{-1}, br, s; 2940 cm^{-1}, w, ν(C–H aliphatic); 2068 cm^{-1} (m, shrp, ν(COOH); 1689 cm^{-1}, 2 unresolved peaks, m, ν(C═O); 1490 cm^{-1} ν(C═C/N), shrp, m) and 1014, 1010 cm^{-1}, ν(C–O/S), where s = strong, w = weak, br = broad, m = medium intensity, and shrp = sharp. The C═C/N/S sp^2-hybridised bonds are signatures of the graphitic cores of the S, N-CDs. Planar and edge defects occur in sp^3-hybridized C–O/N/S groups and are characteristic of CDs, regardless of the carbon source.[19,29,53] Functional groups, such as carboxyl, carbonyl, and hydroxyl groups, on the surfaces of the S, N-CDs enhance their water solubility and hydrophilic interactions. Hence, these groups can act as a pseudo-ligand for cations' electrostatic and non-covalent binding. These interactions are the basis for their solutions being used as reagents for the selective detection of toxic heavy metal ions in aqueous samples.

To confirm the possible interactions between CDs and Cr (VI), FT-IR spectra of pristine S, N-FCDs and ground mixtures of the CDs and Cr(VI) were recorded and are presented in Fig. 2G. Some of the vibrational bands for the CDs/Cr(VI) mixture show shifted and altered peak intensities when compared to those of the CDs alone. These changes correlate with the myriad and non-specific non-covalent interactions between the hard basic groups (C–O/N/S) and the highly electropositive Cr(VI) (a hard Lewis acid), forming semi-stable coordinate complexes. For example, the merged N–H/O–H bands (*ca.* 3500 cm^{-1}) of the CDs/Cr(VI) mixture are slightly shifted to higher frequencies, and are broader and more intense. These differences reflect the mutual electrostatic and unconventional hydrogen bond contacts between Cr(VI) ions and the electron lone pairs of the O–H/N–H groups. Similarly affected vibration bands include the C(O)–O$^-$ (2000 cm^{-1}, shifted $\lambda_{\max}$ and decreased intensity), C═O/S (1700 cm^{-1}, increased intensity), C═N/S (1480 cm^{-1}, increased intensity) and Cr(VI)–N/S-CDs (500 cm^{-1}, shifted $\lambda_{\max}$ and increased intensity). They all attest to mutual interaction between the CD surface donor groups and Cr(VI) ions and whose spectral effects are the basis for the optical sensing of Cr(VI) ions as shall be discussed ahead.

To further investigate the elemental composition and surface functional groups/atomic valence states of the avocado seed-derived S, N-CDs, a photon X-ray spectroscopy (XPS) survey spectrum was recorded. The XPS elemental survey spectrum of the S, N CDs is presented in Fig. 2B; it shows two intense peaks for O 1s (532.2.eV) and C 1s (285.5 eV), with weaker signals for N 1s (399.8 eV), S 2p (163.3 eV), Si 2p (101.5 eV) and P 2p (133.3 eV). Integration of these peaks translates to a composition of 61.7% C 1s, 32.5% O 1s, 3.6% N 1s, 1.44% S 2p, and 0.21% P 2p valence states. The deconvoluted spectra derived from the C 1s peak (Fig. 2E) consist of coalesced peaks at binding energies (eV) of 284.2, 284.6, 286.1, 287.8, and 288.1 eV, due to C–C, C═C(graphitic), C–O/N, C═O, and O–C═O bonds/functional groups, respectively.[54–57] The spectral components of the O 1s peak also confirm the presence of C–O and C═O carboxyl groups, which arise from oxidation reactions enhanced by the acidic 9 M H_2SO_4 synthetic medium. Similar deconvoluted spectra of the N 1s and the S 2p peaks reveal the presence of organic cyanide-like, thiol (mercaptan), and sulfide groups, as shown in Fig. 2B–E. Most of the implied functional groups in the XPS data have been identified and discussed in the FTIR characterisation data, and their presence is consistent with the use of avocado seed extract as a carbon source. The percentage (%) composition of S and N atoms confirms the successful doping of these atoms from the thiosemicarbazide and other nitrogenous sources in the avocado extract. The data confirm the successful formation of nitrogen-doped carbon dots.

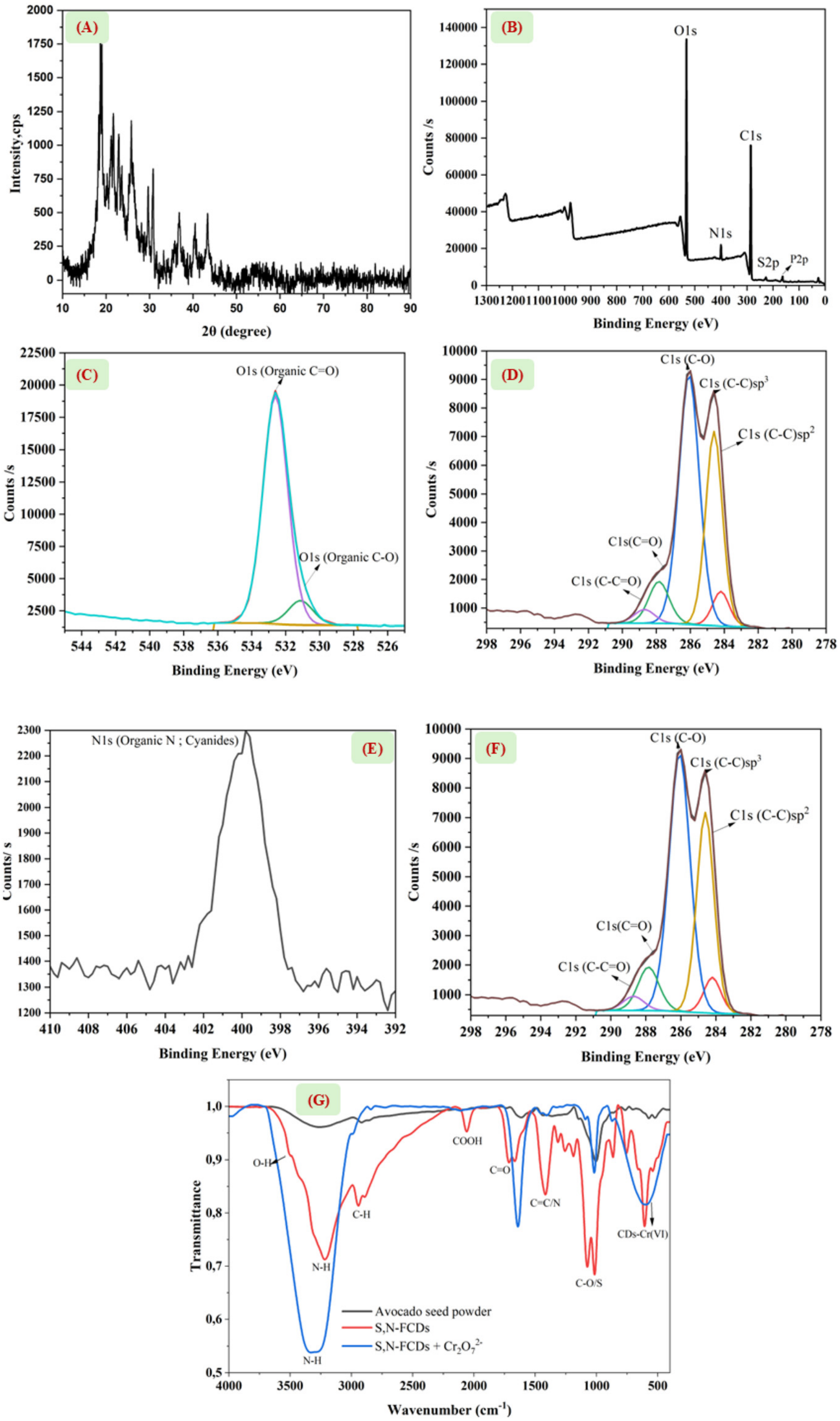

Fig. 2 (A) PXRD with the 2θ-spectrum of the S, N-CDs. (B) XPS survey spectrum of the S, N-CDs, and the deconvoluted spectra of the (C) O 1s, (D) C 1s, (E) N 1s, and (F) S 2p valence states. (G) Overlaid FT-IR spectra of the avocado seed powder extract, S, N-FCDs, and S, N-FCDs mixed with 500 ppb $Cr_2O_7^{2-}$.

3.2 Optical properties of the S, N-CDs

The optical properties of the S, N-CDs were also studied using UV-Visible absorption and fluorescence spectroscopy. After purification using sequential ultracentrifugation, a yellow-coloured and water-soluble nano-colloidal solution of the S, N-CDs was obtained. The UV-visible absorption spectrum is presented in Fig. 3A, featuring a strong absorption band

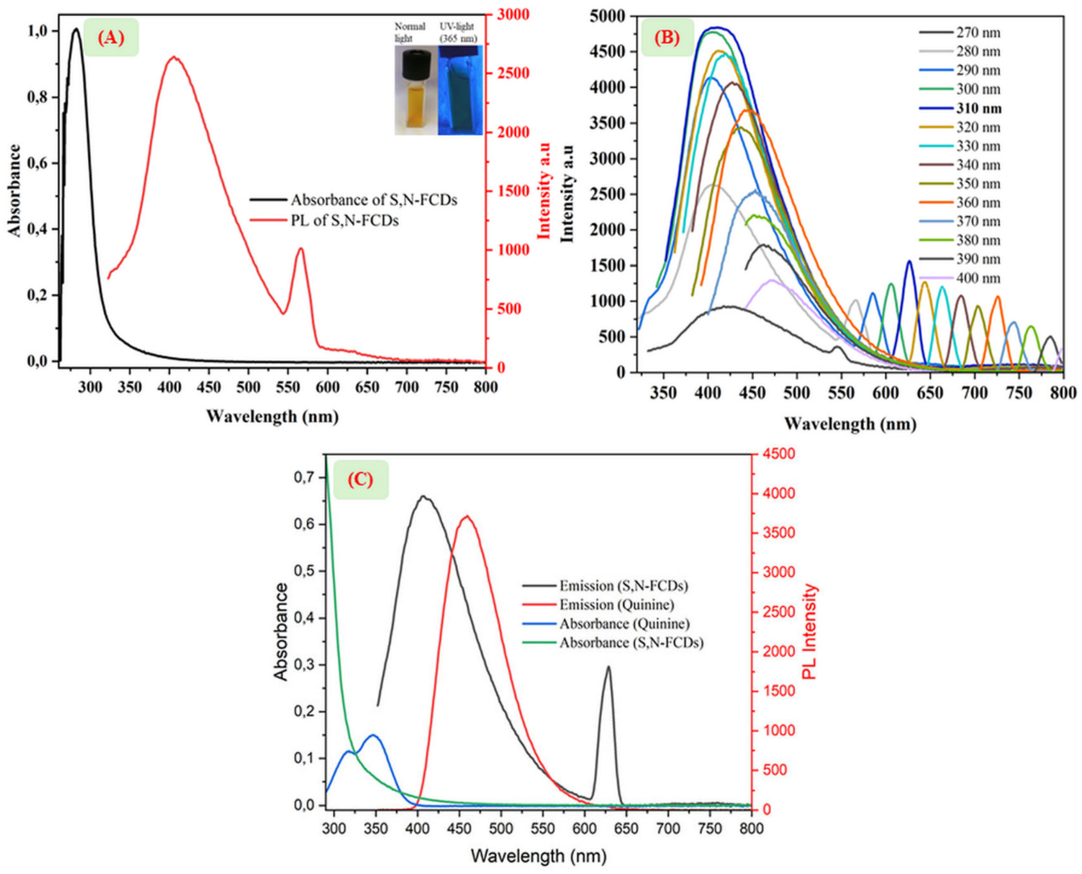

Fig. 3 (A) Stacked UV-visible absorption (black solid line) and fluorescence (FLUOR) (red line) spectra for 8.3 mg L^{-1} S, N-FCDs. The inset image is the visualisation of the S, N-CDs under normal light and 365 nm UV light in the dark. (B) Spectra of the 8.3 mg L^{-1} avocado seed-derived S, N-FCDs at varying excitation wavelengths (270–400 nm, 10 nm intervals). (C) Overlaid UV-Vis and PL spectra of S, N-CDs, and with standard 0.1 M quinine sulfate, from whose data the quantum yield (Q_Y) was calculated.

centred at approximately 280 nm. This is due to the dominant $\pi \rightarrow \pi^*$ electronic transitions of the C=C (sp^2) bonds of the CDs' core or crystalline regions of the graphitic structure. It also features a low molar extinction but a gradually rising band below 400 nm. This band is due to the $n \rightarrow \pi^*$ transition of the various heteroatom (C–O/N/S) functional groups that include hydroxyl/thiols (C–OH/–SH groups), carbonyl/thionyl (C(H)=O/S), and amines (C–NH$_2$), as may occur on the surface of the S, N-CDs derived from biomass. Some important C–X (O, N, S) functional groups, which are well-suited for their sensing capability, have been confirmed in their FT-IR and XPS spectra.

The yellow S, N-CD solution emits a dull green fluorescence as shown (in the inset picture of Fig. 3A) when excited by 365 nm broad UV-Visible radiation from a xenon lamp. Using the data in Fig. 3D, the Q_Y for the avocado-seed-derived S, N-CDs was calculated to be 17.7%. This value is in the middle of the range reported for CDs derived from other natural biomass sources. For example, CDs synthesised from grape seeds by hydrothermal synthesis[21] and avocado seeds by pyrolysis[44] had Q_Y values of 27.7% and 9.2%, respectively.

3.3 S, N-CD host–guest surface interaction absorption (HGSIA) method

3.3.1 Surface interactions and enhanced absorption for the selective detection of $Cr_2O_7^{2-}$. The utilisation of CDs as an optical sensing nanomaterial for Cr(VI) has been extensively reported for interaction-induced fluorescence quenching methods.[58–61] However, the molecular absorption sensing of metal ions by CDs remains relatively unexplored, except for a few recent literature reports.[47–51] Herein, we explore the enhanced absorption and fluorescence quenching methods for dual-mode quantitative Cr(VI) analysis using avocado-derived CDs as pseudo-sensing reagents. To demonstrate the enhanced absorption method, two sets of 200, 500, and 1000 ppb $Cr_2O_7^{2-}$ ions in S, N-CDs and ultrapure water were prepared, and their spectra were recorded, along with those of the S, N-CDs. The overlaid spectra are presented in Fig. 4. As illustrated in the inset to Fig. 4B, the intensities of the absorption bands at 360 nm for $Cr_2O_7^{2-}$ standards (in water) are significantly lower than those in the S, N-CDs. For example, the absorption intensity of the 1000 ppb $Cr_2O_7^{2-}$ in the S, N-CD standard is 14 times higher than that of its counterpart in

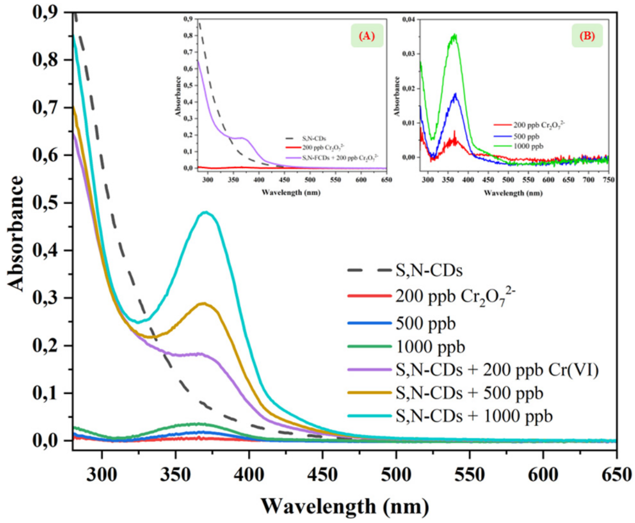

Fig. 4 Overlaid HGSIA UV-visible spectra (band λ_{max} = 375 nm) of the S, N-CD solution; 200, 500 & 1000 ppb Cr(VI) in water (dwarfed bands in the encircled region) and the analogous Cr(VI) standards in S, N-CD solutions. Inset: (A) overlaid spectra of the S, N-CDs, 200 ppb Cr(VI) standard in water and S, N-CD solution showing the absorption enhancement of the dichromate-derived absorption band upon mixing Cr(VI) with the S, N-CDs. (B) Enlarged (zoomed out) overlaid spectra (within the circled range for the absorption band (λ_{max} = 360 nm)) of the 200, 500, and 1000 ppb Cr(VI) standards in ultra-pure water.

ultra-pure water. Considering the spectrum of the CDs as a baseline reference (inset to Fig. 4B), the enhanced absorbance bands of the $Cr_2O_7^{2-}$ ions in S, N-CDs are red-shifted by 15 nm (at 375 nm). These bands also exhibit a linear correlation between absorbance and the increasing concentration of $Cr_2O_7^{2-}$ in S, N-CD standards. These observations suggested that the Cr(VI) ions were involved in surface host–guest interactions with the numerous functional groups on the surface of the avocado seed-derived S, N-CDs, leading to the formation of ground-state coordinate Cr(VI) complexes with enhanced absorptivity at a red-shifted charge transfer (CT) band (375 nm). Hence, these host–guest S, N-CD-Cr(VI) surface interactions that enhanced the absorptivity of Cr(VI) shall be abbreviated hereafter as the 'HGSIA' effect. Although Pizzoferrato and co-workers[47] mentioned and briefly discussed these CD-Cr (VI) interactions, they did not emphasise the origins of the 550 and 700 nm absorption bands used for Cr(VI) quantitation. As already pointed out, and according to the hard–soft acid base (HSAB) theory, the matched atomic orbital energies and sizes of Cr(VI) ions (the hard acids) and the C–O–/N– groups (hard bases) lead to swift interactions between them, marked by significant overlap integrals to form stable ground-state complexes with high molar absorptivities.

The HGSIA effect of the CDs and Cr(VI) ions can be exploited for the detection and quantitative analysis of the latter with some degree of specificity. Thus, we set out to develop and validate a quantitative analytical method for the selective and sensitive detection of Cr(VI) using CDs from avocado seeds. The incorporation of CD from avocado seed makes this HGSIA method eco-friendly and sustainable.

To verify the specificity of the neo-derivatising S, N-CD reagent for $Cr_2O_7^{2-}$ ions, the absorbance at 375 nm for 500 ppb Cr(VI) or other selected metal ions in S, N-CD standards was measured. The overlaid absorption spectra of the CDs, Cr (VI), and mixtures with other metal ions in S- and N-CD solutions are shown in Fig. 5A and C. Their normalised absorbances at 375 nm are depicted as bar graphs in Fig. 5B and D. As illustrated in the bar charts, only the presence of the Mn(VII) ion caused a similar enhancement in the absorbance change of the S, N-CDs as observed for Cr(VI) ions, thereby affecting the specificity and selectivity of the latter. The fact that Cr(VI) and Mn(VII) ions (two highly oxidised ions) induced a similar HGSIA signal in S, N-CDs suggests that their common high oxidation states led to the formation of coordinative complexes of similar stability with CD donor groups. The similarity in the energy and size of their atomic orbitals resulted in similar reactivity towards the C–O/N groups (hard bases) in accordance with the principles of HSAB theory. This is a major limitation regarding the quantitative analysis of Cr(VI) in samples with a high Mn(VII) content. It is noteworthy that Cr(III), the less toxic but lower oxidation state species, does not interfere with Cr(VI) detection, highlighting the speciation specificity capability of this method. When the selectivity evaluation was repeated with the interferent at a 100-fold excess (50 mg L^{-1}), only Fe(II) ions, in addition to Mn(VII) ions (Fig. S3), showed some slight interference. The practical reliability and applicability of the HGSIA mode of detection are limited by a high content of Mn (VII) and Fe(II) ions in real samples. Pretreatment to remove these interferences without altering the integrity of the sample is practically difficult to achieve.

3.3.2 Mechanism of interactions leading to the enhanced absorption of Cr(VI) in S,N-CD medium. Note that only high oxidation state ions, *viz*. Cr(VI) and Mn(VI), induced significant HGSIA changes of the avocado-derived S, N-CDs in solution; the mechanism of their selective detection is likely mediated by the common high positivity and electrophilicity of the metal ions rather than the negative formal charge carried by each of these anionic metal complexes. For example, the non-covalent adduct formed between Cr(VI) and the myriad negatively polarised donor function groups on the surfaces of the S, N-CDs is derived from a pseudo-charge transfer from the lone pairs on the heteroatoms of the S, N-CDs into the low-lying energy vacant d-atomic orbitals of Cr(VI), forming stable and quasi-physicochemical adducts. The strength of the dipolar moment or polarizability of the encounter/adducts is the highest of these two ions due to their high electrophilicity and charge positivity of the metal centres. Resultantly, they form strong steering electric vectors on the incident radiation, causing the observed selective and enhanced absorption bands compared to the absorptivity of their respective neat standards in ultra-pure water.

The nature of the interactions between the surface groups of CDs and responsive metal ions (with which they exhibit selective detection) and detection mechanisms has not been

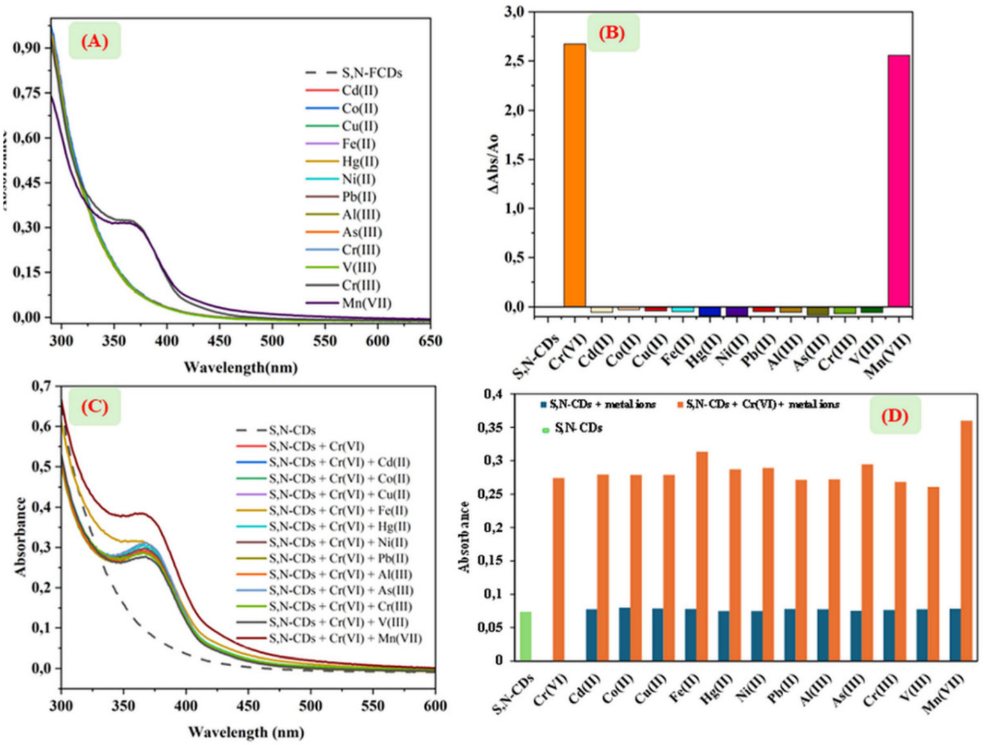

Fig. 5 (A) Overlaid UV-Visible absorption spectra of the 8.3 mg L^{-1} S, N-CDs (2.00 mL) before and after adding 20 μL of 5.00 mg L^{-1} $Cr_2O_7^{2-}$ or selected metal ions (to attain [Cr(vi) or interferent metal ions] of 50 ppb). (B) Bar graphs of the normalised changes in absorption (Δ(Abs/Abs) at 375 nm of the 50 ppb solution of Cr(vi) or interfering metal ions). (C) Overlaid UV-visible absorption spectra of 8.3 mg L^{-1} S, N-CD solution (2.00 mL) before and after the addition of 20 μL of a mixture of 5.00 mg L^{-1} $Cr_2O_7^{2-}$ and 100-fold 500 mg L^{-1} of other metal ions. (D) Bar graphs of the normalised changes in absorption (ΔAbs/Abs) of 0.50 mg L^{-1} solution of Cr(vi) and 50 mg L^{-1} of potential interfering ions.

enunciated more clearly than we are doing here.[47–51] We postulate that the electron-donor of the S, N-CDs (host receptors) forms encounter pairs with the highly positively charged Cr(vi) ions, resulting in adducts with stronger molar extinction absorption coefficients, which leads to absorption enhancement. The formed Cr(vi)-S, N-CD adduct exhibits a stronger electric dipole moment, which enhances absorption and results in a slightly red-shifted wavelength. This results in more intense Cr(vi)-derived absorption peaks compared to the those of dichromate, leading to higher detection sensitivity. Furthermore, the zeta potential measurements of the adulterated S, N-CDs and their mixture with 20 μL of 10 mg L^{-1} of $Cr_2O_7^{2}$ showed a surface charge increase of about 10 mV, changing from −5.66 (± 0.07) mV (for the S, N-CDs) to +4.22 (± 0.05) mV (for the S, N-CDs + Cr(vi)), *vide supra*. The S, N-CDs carry a net negative charge on their surface due to the presence of different electron-donating functional groups. They are dominated by O- and N-containing functional groups (COO–, OH–, NC, and SH), as also corroborated by data from SEM-EDX, XPS, and FT-IR analyses. The increase in the surface charge value for the S, N-CDs + Cr(vi) mixture supports electrostatic interactions that foster strong adsorptive dipolar pairs. These interactions manifest as unusual enhanced absorption of the dichromate ions in S, N-CDs, which forms the detection principle of the newly developed HGSIA method. As already stated, the surface interactions caused an enhancement in the molar absorptivity at a shifted charge transfer band at a λ_{max} of 375 nm (Fig. 4). This confirms that the S, N-CDs interact with Cr(vi) ions on their surface through the HGSIA principles. The principle of detection is the same as that proposed recently by Pizzoferrato and co-workers[47] and is also similar to the calorimetric reference method (EPA Ref. No. 7196A, 1992).[15]

3.3.3 Effect of pH on the HGSIA detection of the Cr(vi) in S, N-CD solution.

The measured absorbance at 375 nm of the Cr(vi)/S N-CD solution at different pH levels shows a slight pH-dependent response in the range of 2–12. The numerous functional groups, such as carboxylic acids, aromatic amines, and phenols/thiols, are protonated/deprotonated to varying degrees depending on their pK_a values. The degree of ionisation of these groups influences the strength of the surface group's interactions. The dipolar moments for the Cr(vi)–CD ion-pairs correlate directly with their enhanced absorption, as shown in the bar charts in Fig. S4. As the CDs become more alkaline, the Cr(vi) absorbance in the S, N-CD media also increases. The deprotonation of acidic groups to form their conjugate groups (*e.g.*, RCO_2^-, RSO_3^-, RNH^- or RNH_2) increases the Cr(vi) ion pair's electric dipole moment. This, together with the delocalisation of electrons *via* resonance and the transfer of electrons from the donor atoms, increases the absorptivity of the adducts.[26,62,63] However, the absorbance beyond pH 10 dropped slightly, possibly due to increasing precipitation of the hydroxide of the solution constituents. Thus, a pH of 9 was considered the optimum pH for evaluating the method.

3.3.4 Linear calibration of Cr(VI) by the S, N-CD HGSIA method. The normalized absorbances measured at 375 nm were plotted against wide-range concentrations ([$Cr_2O_7^{2-}$]) of 0.5–1500 ppb of serially diluted $Cr_2O_7^{2-}$ standards (pH = 9) as shown in Fig. 6. A linear regression (least squares fit) of the normalized absorbance data yielded the calibration equation, $y = 0.0043[\mathrm{Cr(VI)}] + 0.32$, $R^2 = 0.9958$, in the concentration range 0.5–1500 ppb. The calibration graph shows a high sensitivity, high correlation precision, and a wider linear concentration range, 0.5–1500 ppb, compared to other optical absorption methods for $Cr_2O_7^{2-}$ ions.[16,34,50,51] Moreover, ultra-trace concentration limits of detection (LOD) and quantification (LOQ) of 0.14 ppb (2 nM) and 0.47 ppb (9 nM), respectively, for $Cr_2O_7^{2-}$ were estimated by applying replicated ($N = 20$) reagent signal responses (Fig. S12) equivalent to 3- and $10\sigma_{(\mathrm{blank})}$ into the calibration equation, respectively. The values are much lower than those for conventional absorption methods for Cr (VI) ions. For example, direct analysis of $Cr_2O_7^{2-}$ shows narrow linear ranges and poor LODs influenced by the complex ion's pK_a and pH of the medium.[16] A calorimetric method in which Cr(VI) is reduced by *N*,*N*-diethyl-*p*-phenylenediamine showed a linear range of 0.85–60 µM and LOD and LOQ of 0.26 µM (13.5 ppb) and 0.85 µM (21.3 ppb), respectively.[64] The Cr(VI)-hydroquinone-diphenylcarbazide reduction method (adapted from the EPA calorimetric method) depicted a narrow linear range of 0.1–3.0 mg L^{-1}, and LOD and LOQ of 0.07 and 0.1 mg L^{-1} (ppm),[12] respectively, for the determination of ppm levels of Cr(VI) ions after their selective derivatization at pH 2 (λ = 540 nm) by the 1,5-diphenylcarbazide (1,5-DPC) reagent.[15,16] Compared to the EPA method, the new HGSIA method for Cr (VI) ions is highly sensitive (10–100 fold), has significantly lower limits of detection and a wider linear concentration range, as shall be further discussed in the sections ahead. However, its specificity and accuracy are seriously affected by high concentrations of Mn(VII) and Fe(II) ions in the real samples.

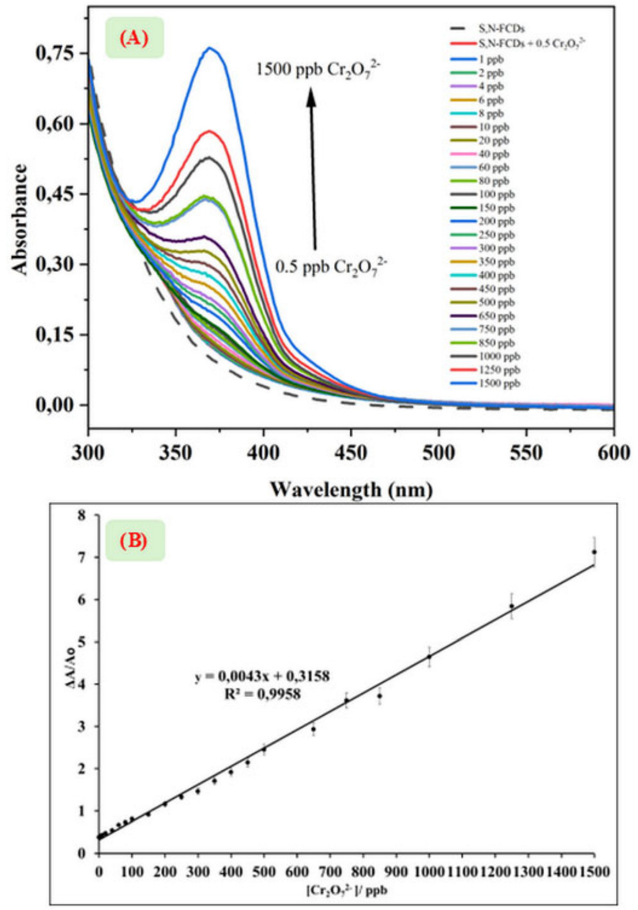

Fig. 6 (A) Overlaid UV-visible absorption spectra of the $Cr_2O_7^{2-}$ ions in S, N-CDs at pH 9 (ammonium buffer) when 20 µL of variable concentrations of $Cr_2O_7^{2-}$ ions were added to 1980 mL of the 8.3 mg L^{-1} S, N-CDs (2.00 mL) to attain final concentrations of 0.50–1500 ppb Cr(VI). (B) The linear calibration plot of normalised absorbance ($\Delta A/A_0$) at 375 nm *versus* $[Cr_2O_7^{2-}]_{\mathrm{ppb}}$.

As already noted, the only other absorption-based calorimetric method for Cr(VI) utilises carbon dots from oxidative etching of fullerenes.[47] A linear concentration range of 1–100 µM and an LOD of 300 nM (15.9 ppb) at a charge transfer band centred at 550 nm were reported (Table 1). Our S, N-CD-HGSIA method presents comparable calibration metrics (a higher calibration slope, lower detection limits, and a wide linear range in the ultra-trace limiting range) when compared to the aforementioned method. Extending the comparison (Table 1) to the CD absorption-based methods for other metal ions, *viz.*, Pb(II),[34] Ag(I),[50] Co(II),[51] and Cu(II),[48,49] the metrics of our method are superior, showing the benefit of using avocado seed as a carbon source, unlike the non-biomass-derived carbon sources used for CD production in all the aforementioned studies. Thus, the superior analytical performance of the HGSIA for Cr(VI) and the sustainability of the S, N-CD sensing reagents make it a ready, viable analytical method for detecting Cr(VI) in the ppb range. To check the accuracy and variability of the HGSIA responses, 100 ppb Cr(VI) was measured repeatedly, $N = 15$ times (Fig. S6), considering it as a sample. Its absorbance values have a 2.7% RSD and a mean signal, equivalent to a concentration of 99.4 ppb Cr(VI) in the calibration equation. These checks verify the high precision and accuracy of the HGSIA method in detecting Cr(VI) in the checked sample. The batch-to-batch reproducibility of the sensitivity of the S, N-CDs towards the Cr(VI) was verified by undertaking the calibration process using S, N-CDs synthesised on different dates, as shown in Fig. S5. A similar linear correlation was demonstrated within the same linear range. In all cases beyond 1500 ppb Cr(VI), the absorbance in the S, N-CDs deviated towards a new response factor with increasing [Cr(VI)].

3.3.5 $Cr_2O_7^{2-}$ (Cr(VI)) analysis in spiked river water samples and dichromate-contaminated laboratory effluent (a positive control sample) using the HGSIA method. Real water samples from the uMsunduzi river were spiked with a fixed

Table 1 Comparison of the CD-based HSGIA-calorimetric quantitative methods for detecting Cr(VI) and other metal ions

Carbon precursor for CDs (non-sustainable sources)	Method of detection (metal ions)	Linear calibration equation (R^2)	Linear range, ppb (μM)	LOD (ppb) (nM)	Ref.
Cr(VI) ion					
C_{60} fullerene carbon (oxidative opening)	CD calorimetric absorption (Cr(VI))	0.00319[Cr(VI)] + 0.000739 (0.9980)	52–5200 (1–100 μM)	15.6 ppb (300 nM) (0.3 μM)	47
na	Calorimetric-*N*-diethyl-*p*-phenylenediamine (Cr(VI))	*y* = 33.594[Cr(VI)] (0.9993)	44.2–3120 (0.85–60 μM)	13.5 ppb (260 nM) (0.26 μM)	64
na	Calorimetric-1,5-diphenylcarbazide (Cr(VI))	*y* = 0.0305[Cr(VI)] (0.9994)	1–800 (1.9–15.4 μM)	1000 ppb (1923 nM) (1.92 μM)	16
Avocado seeds (hydrothermal)	**UV-visible enhanced absorption (HGSIA) (Cr(VI))**	***y* = 0.0043[Cr(VI)] + 0.32 (0.9958)**	**0.5–1500 ppb (0.0096–28.8 μM)**	**0.14 ppb (2.0 nM) (0.00269 μM)**	**This work**
Other metal ions					
Glutathione and formamide (microwave-assisted)	CD calorimetric absorption for Pb(II)	ns	0.21–199 ppb (0.001–0.961 μM)	7.69 ppb (37.1 nM) (0.0371 μM)	34
Benzenetetramine tetrahydrochloride and poly(2-ethy), 2-oxazoline (hydrothermal)	CD calorimetric absorption (Ag(I))	*y* = 4.76 × 10^{-3}[Ag(I)] + 2.69 × 10^{-3} (0.98)	0–41 600 ppb (0–800 μM)	5.39 ppb (50 nM) (0.05 μM)	50
L-Histidine and ethylene imine polymer (hydrothermal)	CD calorimetric absorption (Co(II))	*y* = 1.688 × 10^{-2}[CoII] + 4.447 (0.99)	0–11 786 ppb (0–200 μM)	44.2 ppb (750 nM) (0.75 μM)	51
o-Phenylenediamine and ammonium sulphate	CD calorimetric absorption (Cu(II))	ns	65.5–6555 (1–100 μM)	13.1 ppb (200 nM) (0.02 μM)	48
o-Phenylenediamine and ammonium sulphate	CD calorimetric absorption (Cu(II))	ns	32.8–6555 (1–100 μM)	13.1 ppb (200 nM) (0.2 μM)	49

na = not applicable and ns = not specified.

concentration of S, N-FCDs. The absorbance of the spiked and laboratory wastewater contaminated with $Cr_2O_7^{2-}$ ions (positive control) was measured in replicates and applied directly to the HGSIA calibration equation. The absorbance of the river water was indiscernible, indicating that the concentration of Cr(VI) was below the detection limit or was absent. The absorption spectra of the spiked water samples (after several aliquot additions to attain 0–200 ppb Cr(VI) standards) are shown in Fig. S7. A standard addition plot of the normalised absorbance *versus* [Cr(VI)] is linear, indicating a precise linear correlation between the two variables, as observed in the external calibration approach. The normalised absorbances at 375 nm of two of the standard additions with final concentration levels of 20 ppb and 200 ppb Cr(VI) ions in S, N-CD solutions were substituted into the external calibration equation to deduce the respective measured (recovered) concentration of Cr(VI). The recovery (%) values of $Cr_2O_7^{2-}$ in the spiked uMsunduzi River at the two chosen spiked levels are presented in Table 2. High Cr(VI) percentage recoveries of 94% and 98% were demonstrated for the 20 and 200 ppb Cr(VI) standards, respectively. This means that the HGSIA (Cr(VI) in S, N-CDs) method is highly accurate even at the ppb level. According to the World Health Organisation (WHO) safety regulations, Cr(VI) concentrations at or below 50 mg L^{-1} (approximately 900 nM) are considered tolerable and permissible in water supply resources. Thus, the new HGSIA-Cr(VI)-S, N-CD method is sensitive enough to monitor Cr(VI) even at concentrations well below the permissible levels in natural and drinking water set for monitoring and regulation by the World Health Organization (WHO),[65] USEPA,[15] and South African standards.[66] The regulated concentrations of total Cr in natural and drinking water are set at a threshold of ≤50 ppb (0.960 nM L^{-1}).

The recoveries in a river water sample are comparable with those obtained using ICP-OES, for which 91.5% and 103.6% were deduced, respectively. Moreover, as shown in Fig. S8, the analysis of a dichromate-contaminated laboratory waste sample (positive control sample) gave a concentration of 474 ppb $Cr_2O_7^{2-}$ using the HGSIA calibration equation, which compares well with the ICP OES's result of 450 ppb. In both cases, the positive control sample had to be diluted 3 times.

3.4 S, N-FCD fluorescence (FLUOR) quenching by the Cr(VI) method

3.4.1 Excitation wavelength-dependence of S, N-FCD FLUOR. The emission spectra of the yellow S, N-FCD solution

Table 2 Recoveries of Cr(VI) ($Cr_2O_7^{2-}$) ions in the uMsunduzi river sample and quantitative positive control (laboratory effluent) using the HGSIA method

	[$Cr_2O_7^{2-}$], ppb		% Recovery	%RSD (*N* = 3)
	Added	Measured		
uMsunduzi River water	20	19.2	96%	± 2.4
	200	196.3	98%	± 1.6
Lab effluent	—	475		± 2.8

(as seen under normal light) were recorded as a function of the excitation wavelength in the range 270–400 nm at 10 nm intervals. The overlaid spectra are presented in Fig. 3A and B. The spectra have two emission peaks at 420 nm (broad and strong) and 610 nm (sharp and minor), implying the existence of dual emissive states in their excited states. The mixing of the blue colour hue (major peak at 420 nm) and yellow hue (minor peak at 610 nm) gives rise to the dull green colour of the fluorescence of the CDs when observed under UV light irradiation. When the S, N-FCDs are excited by UV radiation (λ = 270–400 nm), emission spectra comprising two emission bands are observed, with fluorescence emission wavelengths and intensities varying with the excitation wavelength. The intensities of the emission reach a maximum at 420 nm for the major and shorter wavelength (higher energy) when an excitation wavelength of 310 nm is used. A similar trend is observed for the minor peak at 625 nm when the 310 nm radiation is used. The major emission band is broader, occurring in the 390–550 nm range, while a minor and narrower band is featured in the wavelength range of 565–800 nm. The two characteristic emission peaks indicate two emissive states (for size distribution, refer to Fig. 1C) of the avocado seed-derived FCDs, which contribute to the green hue upon excitation with UVC light. The broad and higher energy emission band (range: 390–550 nm) is likely due to the smaller-sized CDs, which have characteristically wider band gap energies.

The emission wavelengths of these FCDs are therefore dependent on the excitation wavelength. This is a testament to the variable energy (emissive) states of the S, N-FCDs as controlled by the variable sizes and the associated quantum confinement properties of the biomass-derived CDs. This corroborates the HRTEM data, which show that the S, N-FCDs have a variable size range of 8.5–18 nm, unlike the fluorescence of CDs derived from synthetic chemicals (such as citric acid, glucose, *etc.*), which serve as the carbon sources.[20,43,44,55,67–70] The use of the avocado seed as a carbon source resulted in CDs with an even wider diversity of natural domain surface functional groups (–C(O)═O/S, –C–OH, and $-CNH_2$), which shifted the absorption band to higher wavelengths. Consequently, our avocado-seed-derived fluorescent carbon dots (FCDs) had a green emission hue and a relatively lower energy band gap. The S, N-FCDs exhibit dual emissive states with two different band gaps, resulting in two emission peaks upon excitation.

3.4.2 Stability of the fluorescence emission of the S, N-FCDs. Repeated fluorescence measurements of the S, N-CD solution under constant irradiation with 365 nm radiation for 3 h showed a gradual decrease in the fluorescence intensity of about 34% (see Fig. S9A and B). Under prolonged UVC-light exposure, the photolytic degradation of the CD emissive states affects the emission stability of the S, N-FCD. In such applications, the bleaching effect may degrade the S, N-FCDs, thereby affecting their function. However, this is of little concern in fluorometric sensing, where full spectrum acquisition is complete within 120 s, for which the decrease is negligible. The fluorescence stability of the FCDs was also monitored in the presence of increasing concentrations (0.2–1.0 M) of H_2O_2 to probe the effect of mild oxidising conditions on the surface groups of the S, N-FCDs in solution. Only a 30% decrease in FLUOR intensity was observed when the $[H_2O_2]$ was increased five times, as shown in Fig. S10C and D. Thus, only in aggressively oxidising media (or equivalent) in the natural environment can the FLOUR signals of the S, N-FCDs become unreproducible towards Cr(VI) detection. When the oxidising agent was replaced with a high ionic strength salt of variable concentration (0.2–0.4 M NaCl), the fluorescence of the S, N-FCDs was not significantly altered (Fig. S10A and B), indicating excellent ionic salt resistance and tolerance. In different pH buffers (2–12), the FLUOR of the S, N-FCDs increased gradually up to 9 before it decreased slightly beyond pH 10, as shown in (Fig. S9C and D). The FLUOR of the S, N-FCDs shows excellent stability after storage and daily measurements for 30 consecutive days, with a slight decrease in intensity.[14,18,30,63,70,71]

3.4.3 Quenching of the S, N-FCD fluorescence by Cr(VI)

3.4.3.1 Evaluating the selectivity of the detection method. The fluorescence of the S, N-FCDs at 420 nm after excitation at 310 nm in the presence of Cr(VI) and other selected metal ions was significantly quenched only by the Cr(VI) and Mn(VII) ions, with close to 85% and 77% reduction of the initial intensity, respectively, as depicted in Fig. 7. The high selectivity and specificity of these green carbon source (avocado seed)-derived CDs for Cr(VI) ions are intriguingly similar to those of the HGSIA method. Thus, these avocado seed-based CDs are a sustainable, neo-sensing fluorescent reagent for the comparative detection and quantitative analysis of Cr(VI) ions in aqueous media. Thus, they exhibit a convenient dual-mode for sensing Cr(VI) *via* both fluorescence quenching (FLUOR) and HGSIA methods. This makes them attractive analytical reagents for routinely monitoring Cr(VI) contamination *via* two independent methods whose output data can be juxtaposed and conveniently compared. This presents an opportunity to cross-validate the analytical data and method performance, particularly in cases involving the analysis of complex matrices in natural aquatic environments.

Thus, we set out to validate the analytical performances of the fluorescence (FLUOR) quenching method as we had done for the HGSIA method. Further experiments on the specificity of detection and quantitative aspects of the Cr(VI) FLUOR quenching method were conducted. The measurements of the quenched FLUOR were repeated in the presence of binary mixtures of Cr(VI) and other metal ions at 1 : 1 and 1 : 100-fold concentration ratios. The emission spectra and the quenched FLUOR data at 420 nm for the latter are presented in Fig. S11. The extent of quenching by Cr(VI) mixtures in the presence of another metal ion remained unchanged except for Mn(VII) ions. The results also demonstrated that Mn(VII) is a potential fluorescence quenching interferent, particularly in samples with high ion concentrations. Noteworthily, the quenching of the FLUOR is sensitive to the high oxidation states of Cr or Mn metal ions, *i.e.*, as Cr(VI) and Mn(VII).

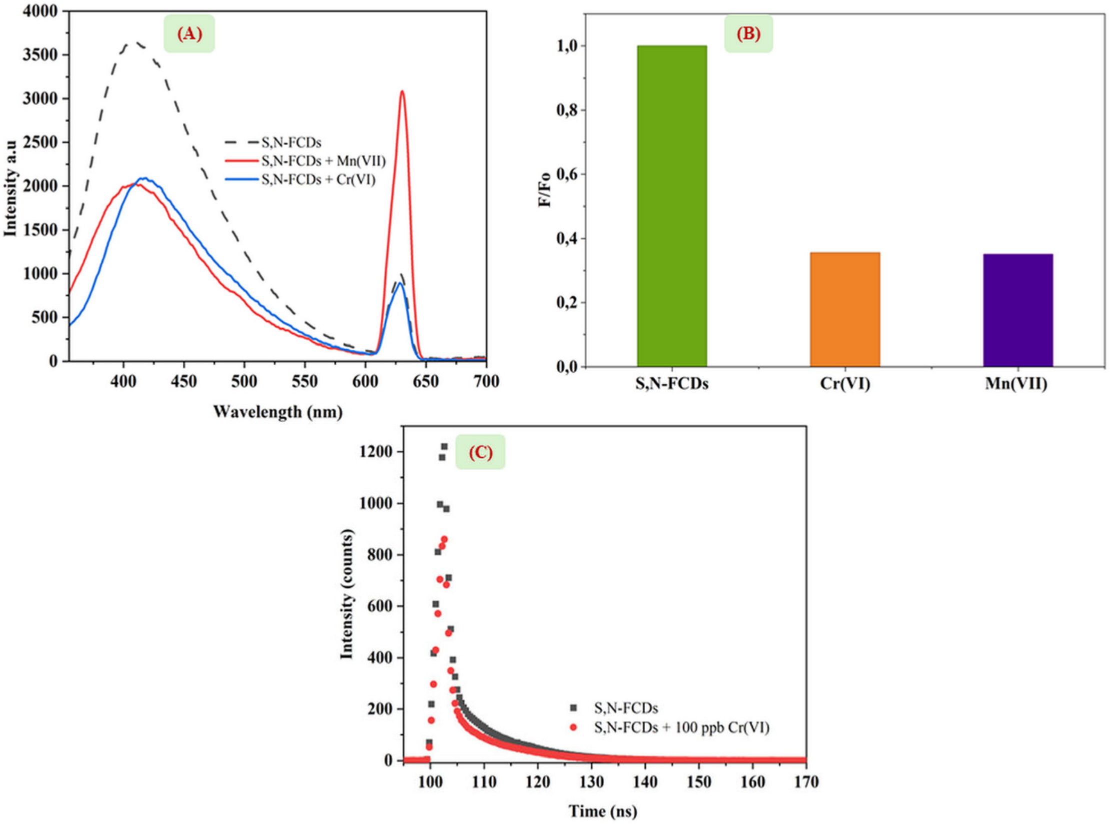

Fig. 7 Overlaid PL spectra of 8.3 mg L^{-1} of S, N-FCDs (2.00 mL), showing quenched fluorescence when mixed with 20 µL of 100 mg L^{-1} Cr(vi) and Mn(vii) ions. (B) Bar graph of S, N-FCDs with Mn(vii) and Cr(vi) ions. (C) Fluorescence lifetime decay profiles of N, S-CDs before (black) and after (red) Cr(vi) addition.

We proceeded to calibrate the fluorimeter for the quantitative analysis of Cr(vi) using quenched fluorescence, enabling us to conduct a comparative analysis with HGSIA data regarding their quantitative analytical performances.

3.4.3.2 Quantitative analysis of Cr(vi) by the S, N-FCD quenching method: Calibration aspects. The S, N-FCDs, and Cr(vi) in S, N-FCD standards were prepared using methods similar to the HGSIA method. Their spectra were recorded as overlays and are presented in Fig. 8A. A plot of the normalised intensity (F_0/F) and the [Cr(vi)] (Fig. 8B) yielded a linear Stern–Volmer equation: $y_{(F_0/F)} = 0.0013[\mathrm{Cr(vi)}] + 1.0982$, $R^2 = 0.9885$ in the linear range of 20–1500 ppb. The Cr(vi) LOD and LOQ values were estimated as 5.9 (11.3 nM) and 25 ppb (48 nM), respectively, from the replicated analysis (Fig. S12B) of the reagent blank ($N = 10$).

As observed for the HGSIA method, the linear concentration range for the Cr(vi) FLUOR quenching by sustainable FCDs in the lower ultra-trace levels of Cr(vi), is nearly two orders of magnitude wide and unprecedented.[46,72] Moreover, the carbon source (avocado seed CDs) used to produce the FCDs is regarded as 'green'. Importantly, the correlation between the response and [Cr(vi)] remains linear over a wider and increasing concentration range (in the ppb range), which may be due to the numerous diverse functional groups and active sites (host receptors) derived from the myriads of precursor molecules in avocado seed extract.

Previously reported optical methods (both fluorescence quenching and absorption/calorimetric) for the quantitative analysis of Cr(vi) using carbon dots derived from both synthetic compounds and biomass are summarised in Table 1. The new avocado CD-based HGSIA method combines a high calibration slope, a wide linear range (0.5–1500 ppb), and low (0.14 ppb) detection limits that compare well with those of the reported methods in Table 4, regardless of the mode or source used to form the CDs.

The calibration data for the quantitative analysis of Cr(vi) ions by previous CD-based fluorometric methods[33,43,44,57,73] are also presented in Table 3. There is wider variability in the analytical performances (calibration slope, linear ranges, and LOD/LOQ values) for CDs derived from biomass sources. The sensitivity and estimated LOD and linear range for the fluorometric detection of Cr(vi) are comparable to those for most of the methods listed in Table 3 for CDs from both sustainable[10,58,59,74–76] and synthetic carbon sources.[77,78] The estimated ultralow LOD of 0.07 nM (0.036) ppb reported by Ávila *et al.*[44] using FCDs from the pyrolysis of an avocado seed powder at 600 °C is much lower than those for the current method. However, the linear range (30–200 µM), while wider,

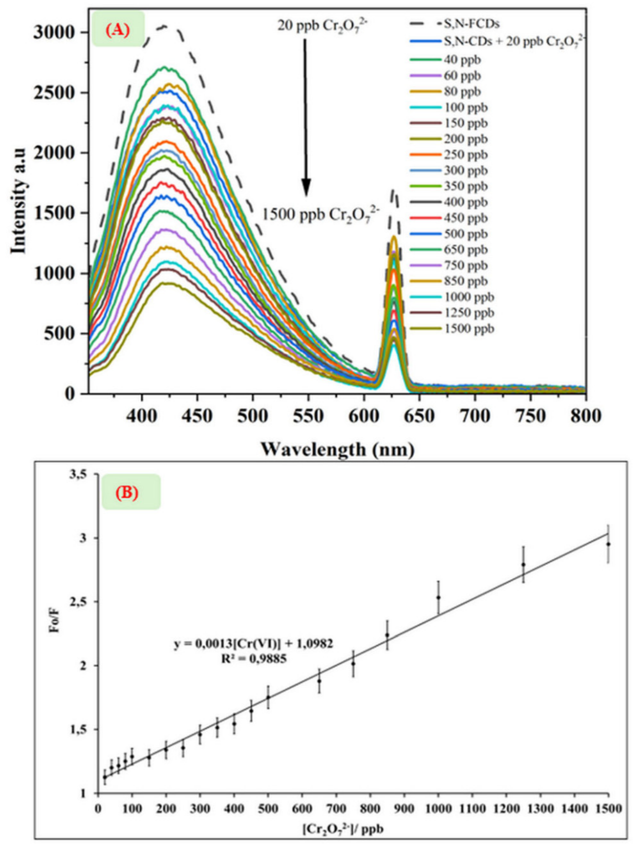

Fig. 8 (A) Overlaid quenching emission spectra of 8.3 mg L^{-1} of S, N-FCDs upon titrating with different concentrations (20–1500 ppb) of $Cr_2O_7^{2-}$ (Cr(VI)). (B) Linear calibration (Stern–Volmer) plot of (F/F_0) *vs* $[Cr_2O_7^{2-}]$ (20–1500 ppb).

is significantly higher than that for our method. In another study, Mandal[59] and co-workers used FCDs from garlic peels to quantify Cr(VI), in the range 7–100 μM (364–5200 ppb), declaring an LOD value of 91.5 ppb, which is higher than that of our fluorometric quenching method. The LODs and linear ranges for Cr(VI) by the FCDs derived from Tulsi leaves,[33] lemon peel,[73] pineapple juice,[43] and winter-sweet flowers,[61] all synthesised hydrothermally, show close variability between them, reflecting the dependence of these parameters on the carbon sources. Most of the LOD values for Tulsi leaves (4.50 ppb), lemon peel (3.80 ppb), pineapple juice (2.70 ppb) and winter-sweet flowers (3.64 ppb) are slightly better than the estimated value of 5.9 ppb by our method.

The synthesised S, N-CDs from avocado seeds showed high accuracy in the analysis of Cr(VI)-spiked and positive check samples. Their performance was similar to that in the HGSIA absorption method, making the dual monitoring and quantitative analysis of Cr(VI) possible. The major drawback of this method is its lack of specificity due to similar responses towards Mn(VII) ions. Surprisingly, this FLUOR quenching method has slightly poorer and higher detection limits than those for the newly developed HGSIA Cr(VI) method. This emphasises the higher sensitivity of the S, N-CDs towards Cr (VI) when used as pseudo-derivatising reagents for the HGSIA absorption method.

3.4.3.3 $Cr_2O_7^{2-}$ (Cr(VI)) analysis in spiked river water samples and dichromate-contaminated laboratory effluent (a positive control sample) using the FLUOR quenching method. Real water samples from the uMsunduzi river and laboratory wastewater contaminated with $Cr_2O_7^{2-}$ were spiked at two concentration levels of 20 and 200 ppb Cr(VI), and their intensities were measured by applying the fluorescence quenching calibration equation. The water sample yielded an indiscernible fluo-

Table 3 Comparison of CD-based fluorescence quenching methods for the detection and quantitative analysis of Cr(VI)

Carbon precursor for CDs (synthetic method)	Method of detection	Stern–Volmer equation (R^2)	Linear range, ppb (μM)	LOD, ppb (nM) (μM)	Ref.
Avocado seeds (pyrolysis at 600 °C)	Fluorescence quenching	$y = 6.529 \times 10^{-3}$ [Cr(VI)] + 1.31 (0.9954)	1560–10 400 ppb (30–200 μM)	0.036 ppb (0.07 nM) (7×10^{-5} μM)	44
Lemon peel (hydrothermal)	Fluorescence quenching	$y = 0.1024$[Cr(VI)] + 0.4573 (0.9542)	130–2600 ppb (25–50 μM)	3.8 ppb (73 nM) (0.073 μM)	73
Pineapple juice (hydrothermal)	Fluorescence quenching	ns (0.9956)	0–936 ppb (0–18 μM)	2.70 ppb (5.1 nM) (5.1×10^{-4} μM)	43
Tulsi leaves (hydrothermal)	Fluorescence quenching	$y = 0.19197 + 1.0632$ (0.9973)	83–2600 ppb (1.6–50 μM)	4.5 ppb (8.6 nM) (0.0086 μM)	33
Chrome shavings (hydrothermal)	Fluorescence quenching	$y = 2.29 \times 10^{-3}$[Cr(VI)] + 1.346×10^{-3} (0.992)	0–13 000 ppb (0–250 μM)	72.8 ppb (1400 nM) (1.4 μM)	58
Flowers of winter-sweet (hydrothermal)	Fluorescence quenching	$y = 6 \times 10^{3}$[Cr(VI)] + 0.175 (0.994)	5.2–3120 ppb (0.1–60 μM)	3.64 ppb (70 nM) (0.07 μM)	61
Citric acid and urea (hydrothermal)	Fluorescence quenching	ns (0.9974)	26–2600 ppb (0.5–50 μM)	3.80 ppb 73 nM (0.073 μM)	77
Garlic peel (hydrothermal)	Fluorescence quenching	ns (0.9942)	364–5200 ppb (7–100 μM)	95.2 ppb (1830 nM) (1.83 μM)	59
Longan peel and ethylenediamine (hydrothermal)	Fluorescence	$y = 3.11 \times 10^{-3}$[Cr(VI)] + 1.008 (0.9919)	1040–10 400 ppb (20–200 μM)	72.8 ppb (1400 nM) (1.4 μM)	60
Avocado seeds (hydrothermal)	**Fluorescence quenching**	**$y = 1.3 \times 10^{-3}$[Cr(VI)] + 1.0982 (0.9885)**	**20–1500 ppb (0.38–28.8 μM)**	**5.9 ppb (113 nM) (0.113 μM)**	**This work**

ns = not specified.

rescence quenching signal, indicating that the concentration was below the detection limit. The water sample was then spiked at two concentration levels as performed for the HGSIA method. The absorbances of spiked samples (20 and 200 ppb Cr(VI) in S, N-FCDs/river water) were measured at 420 nm. The recovery values (%) were found to be 89% and 94% at each spiked level and are presented in Table 4. The FLUOR quenching method has good recoveries, although they are lower than those of the HGSIA method. However, they are comparable to those of ICP-OES (Fig. S13). The positive control sample, which was contaminated with Cr(VI), was also analysed using the FLUOR quenching method, which showed a much lower concentration than that of HGSIA, which was found to be 412 ppb. This makes the HGSIA method relatively more specific for Cr(VI), resulting in better recoveries and accuracy than the FLUOR quenching method.

3.5 Possible Cr(VI) sensing mechanism using S, N-CDs (FLUOR quenching method)

There are numerous possible mechanisms by which the FLUOR of these green S, N-FCDs can be quenched by metal ions such as Cr(VI) ions. We have just demonstrated that the selective and enhanced absorption (HGSIA) method between the Cr(VI)-S, N-CDs is based on the host–guest interactions between the functional groups of the latter and the Cr(VI) ions. The larger steering dipolar moment in the adducts causes an enhanced absorbance and a slight red shift. This increases the sensitivity of the absorption method towards Cr(VI) ions compared to that of the calorimetric method for the same analyte. The same interaction effects indicate that upon excitation of the S, N-CDs in the presence of Cr(VI) ions, the fluorescence of the former is quenched by the enhanced absorption of the Cr(VI) due to the overlap in the emission and absorption bands. The quenching phenomenon is called the Inner Filter Effect (IFE) and has been widely reported in the literature for the selective detection of Cr(VI) or other metal ions.[37,42,43,45,46,56,79–84] The inner filter effect and the dipolar interaction manifest in an increase in the zeta potential before and after mixing the S, N-FCDs with Cr(VI), as discussed for the HGSIA (*vide supra*). Addition of the highly electropositive and highly oxidised Cr(VI) ions to the S, N-FCDs with a net surface potential of −5.66 (±0.07) mV increases the potential to 4.22 (±0.05) mV, triggering an inner filter (absorption) effect on the mixture, which also quenches the FLUOR of the CDs. Thus, the somewhat overlapping mechanisms of Cr(VI) sensing by the FLUOR quenching and HGSIA methods are illustrated in the two schematic analytical sensing routes for Cr(VI) shown in Scheme 2. The absorption/emission band overlap is described in the PL decay plots shown in Fig. S12C. The resultant inner filter (self-FLUOR quenching by enhanced absorption) is, by implication, the primary mechanism by which these neo-derivatising FCDs selectively sense the Cr(VI). As depicted in Fig. 7C, the addition of Cr(VI) to the CDs shortens their fluorescence lifetime as depicted in the increased curvature of the decay plot. At the same time, the emission intensity

Table 4 Recoveries of $Cr_2O_7^{2-}$ ions in the uMsunduzi river sample and quantitative positive control (laboratory effluent) using the FLUOR quenching method

	$[Cr_2O_7^{2-}]$, ppb			% RSD
	Added	Measured	% recovery	(N = 3)
uMsunduzi river water	20	17.8	89%	± 4.7
	200	188.9	94%	± 1.2
Lab effluent	—	412		± 5.3

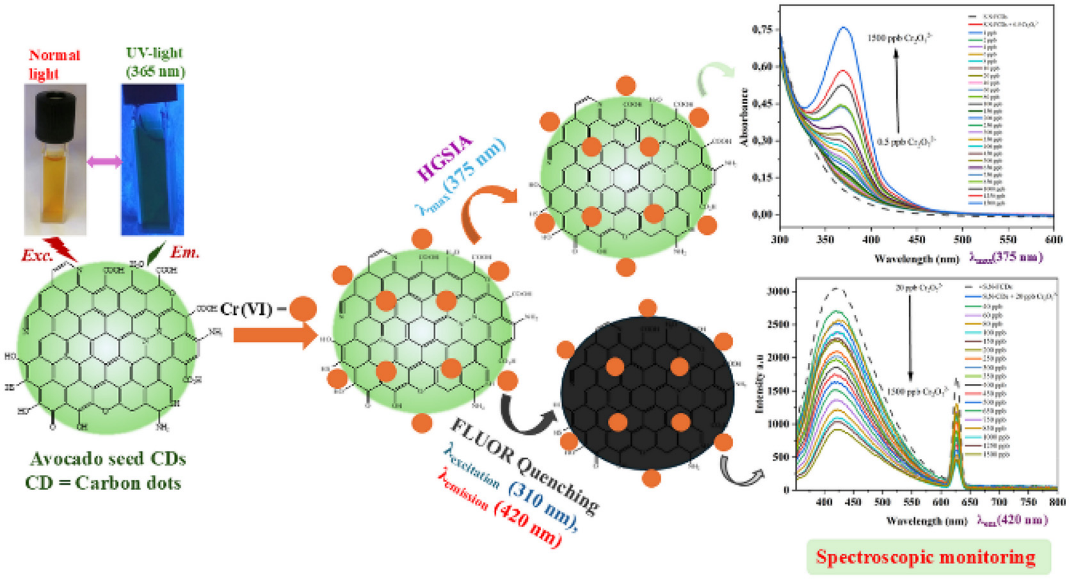

Scheme 2 Possible sensing mechanisms of the S, N-CDs with $Cr_2O_7^{2-}$ *via* the HGSIA and FLUOR quenching methods, the latter depicting the inner filter effect as a possible sensing mechanism.

for the S, N-FCDs is decreased. Both changes are characteristic of quenching of the CD emission by an IFE, induced by the dynamic interactions between the Cr(VI) and the donor groups of the CDs, as also reported in other studies.[37,44,46,85] The IFE accounts for the enhanced molar absorptivity of the charge transfer bands that are exploited for the sensitive detection and quantitative analysis of Cr(VI) in the HGSIA mode, making dual mode detection possible. Moreover, the SEM image of the S, N-FCDs mixed with 20 μL of 0.5 mg L^{-1} Cr(VI) (Fig. S2) appears as a smooth, diffuse grey image (possibly due to the reduced emission brightness of the CDs) compared to the S, N-FCDs alone. The host–guest interactions of Cr(VI) on the donor groups on the FCDs enhance the inner filtering and quenching of the FLUOR emission of the host, thereby dimming the brightness contrast in the SEM measurement. Because the absorption of the guest Cr(VI) ions in S N-CDs occurs by the enhanced surface interactions (the HGSIA method), it quenches the FLUOR by the same margin. Thus, the effect of Cr(VI) on the emissive states of functional groups is similar to what was reported for Fe(III).[86] Another plausible mechanism for FLUOR quenching is CD aggregation-induced quenching, similar to what has been proposed for quenching by Fe(II) ions.[84] As the concentration of the Cr(VI) (quenching ions) increases, it induces surface charge neutralisation and ultimate aggregation and coalescence that rapidly extinguish the emissive state of the FCDs.

4. Conclusions

In this study, two quantitative methods for Cr(VI) based on enhanced absorption and fluorescence quenching have been developed and validated for the quantitative analysis of chromium(VI) ions using avocado seed-derived carbon quantum dots (S, N-CDs) as pseudo-derivatising reagents. The S, N-CDs selectively detect Cr(VI) by the enhanced absorption at Cr(VI)'s charge transfer band ($\lambda_{\max} = 375$ nm) as well as by fluorescence quenching at 420 nm. For both modes, Mn(VII) ions strongly interfere with the Cr(VI) detection. At pH 9, the enhanced absorption method showed a linear correlation with the [Cr(VI)] range of 0.5–1500 ppb, yielding estimated LOD and LOQ values of 0.14 ppb and 0.49 ppb, respectively. The green fluorescence of the S, N-CDs is also selectively quenched by the Cr(VI) ions and Mn(VII) ions. The quenching of the S, N-CD fluorescence linearly varied with the [Cr(VI)] concentration in the range of 20–1500 ppb, yielding estimated LOD and LOQ of 5.9 and 25 ppb from replicated analysis of the CDs as a reagent blank. Both methods showed good recovery (89–99%) for ppb levels of Cr(VI) spiked in uMsunduzi river water samples. The methods could detect Cr(VI) in a laboratory waste sample (positive control) with good comparability and accuracy compared to the ICP-OES result. Thus, these two methods, employing the S, N-FCDs derived from avocado seeds as pseudo-sensing reagents, can be used for the quantitative detection of Cr(VI) ions at the ppb levels, surpassing conventional calorimetric detection of Cr(VI) after derivatisation.

Author contributions

AM: laboratory Investigations, data analysis and visualisation, data curation, drafting, and review. XN: data validation, writing, and review. INB: research supervision, resourcing, data validation, writing, and review. AM: conceptualisation, funding acquisition, resourcing and administration, research supervision, data validation, writing, and review.

Conflicts of interest

There are no conflicts to declare.

Data availability

The data used in the article are available upon request from the authors.

Supplementary information (SI) is available. The SI file contains supplementary procedures on the preparation of avocado seed powder, evaluation and optimization of the optical properties of S, N-C-dots, and method development and validation for Cr(VI) sensing by both enhanced absorption and fluorescence quenching modes of detection. It also contains elemental mappings and SEM-EDX images of the S, N-C-dots, Figures and tabled data on the extra evaluations on the analytical performance of S, N-C-dots towards Cr(VI) ions for both modes. See DOI: https://doi.org/10.1039/d5nr04174k.

Acknowledgements

This study was funded by the National Research Foundation (NRF) of South Africa and the University of KwaZulu-Natal. The authors are grateful to the South Africa Council for Scientific and Industrial Research (CSIR) Inter-Programme Bursary Scheme for financial support of a 2025 MSc bursary to Amahle Mkhize. We thank UKZN's Microscopy and Microanalysis Unit (MMU), UKZN's School of Pharmaceutical Sciences, College of Health Sciences, and the National Metrology Institute of South Africa (NMISA) for electron microscopy, zeta-potential, and XPS analyses, respectively. The views expressed are those of the authors and should not be attributed to the University of KwaZulu-Natal, NRF, or CSIR.

References

1 A. Zhitkovich, *Chem. Res. Toxicol.*, 2011, **24**, 1617–1629.
2 T. O. Ajiboye, O. A. Oyewo and D. C. Onwudiwe, *Chemosphere*, 2021, **262**, 128379.
3 J. A. Jacobs and S. M. Testa, *Chromium(VI) handbook*, 2005, pp. 1–21.
4 M.-N. Georgaki and M. Charalambous, *J. Water Health*, 2023, **21**, 205–223.

5 M. N. Chollom, G. C. Adeyinka and B. F. Bakare, *Int. J. Environ. Anal. Chem.*, 2023, 1–19.

6 J. Beukes, P. Van Zyl and M. Ras, *J. South. Afr. Inst. Min. Metall.*, 2012, **112**, 347–352.

7 M. Loock-Hattingh, J. Beukes, P. Van Zyl and L. Tiedt, *Metall. Mater. Trans. B*, 2015, **46**, 2315–2325.

8 S. P. du Preez, T. P. van Kaam, E. Ringdalen, M. Tangstad, K. Morita, D. G. Bessarabov, P. G. van Zyl and J. P. Beukes, *Minerals*, 2023, **13**, 809.

9 M. Loock, J. Beukes and P. Van Zyl, *Water SA*, 2014, **40**, 709–716.

10 N. Kohama, T. Okazaki, K. Sazawa, N. Hata, H. Kuramitz and S. Taguchi, *Anal. Sci.*, 2023, **39**, 857–865.

11 W. Meng, X. Bai, B. Wang, Z. Liu, S. Lu and B. Yang, *Energy Environ. Mater.*, 2019, **2**, 172–192.

12 H. Sulistyarti, P. M. Sari, R. Retnowati, H. Tolle and A. Wiryawan, *IOP Conf. Ser.: Mater. Sci. Eng.*, 2020, **833**(1), 012048.

13 H.-y. Yang, Z.-z. Chen, D.-y. Qi, Y.-j. Deng, Z.-x. Liu, M.-y. Cao, C.-y. Shao and L.-r. Yang, *J. Alloys Compd.*, 2021, **876**, 160115.

14 H.-Y. Kuang, X.-Y. Yuan, L. Feng, H.-W. Huang, C.-R. Tang, K.-Q. Deng and Y.-L. Zeng, *J. Chil. Chem. Soc.*, 2015, **60**, 2840–2842.

15 United States Environmental Protection Agency (U.S. EPA Cr(VI) Standard), 1992.

16 A. Sanchez-Hachair and A. Hofmann, *C. R. Chim.*, 2018, **21**, 890–896.

17 S. Huang, H. Qiu, F. Zhu, S. Lu and Q. Xiao, *Microchim. Acta*, 2015, **182**, 1723–1731.

18 Y. Sun, X. Wang, C. Wang, D. Tong, Q. Wu, K. Jiang, Y. Jiang, C. Wang and M. Yang, *Microchim. Acta*, 2018, **185**, 1–8.

19 L. Xia, X. Li, Y. Zhang, K. Zhou, L. Yuan, R. Shi, K. Zhang and Q. Fu, *Molecules*, 2022, **27**, 1258.

20 V. Sharma, S. K. Singh and S. M. Mobin, *Nanoscale Adv.*, 2019, **1**, 1290–1296.

21 J. Li, O. Xu and X. Zhu, *RSC Adv.*, 2021, **11**, 34107–34116.

22 J. Zhang and S.-H. Yu, *Mater. Today*, 2016, **19**, 382–393.

23 Y. Lou, X. Hao, L. Liao, K. Zhang, S. Chen, Z. Li, J. Ou, A. Qin and Z. Li, *Nano Sel.*, 2021, **2**, 1117–1145.

24 M. K. Chini, V. Kumar, A. Javed and S. Satapathi, *Nano-Struct. Nano-Objects*, 2019, **19**, 100347.

25 M. Jorns and D. Pappas, *Nanomaterials*, 2021, **11**, 1448.

26 N. De Acha, C. Elosúa, J. M. Corres and F. J. Arregui, *Sensors*, 2019, **19**, 599.

27 A. Durairaj, M. Maruthapandi, J. H. Luong, I. Perelshtein and A. Gedanken, *ACS Appl. Bio Mater.*, 2022, **5**, 5790–5799.

28 Q. Xu, T. Kuang, Y. Liu, L. Cai, X. Peng, T. S. Sreeprasad, P. Zhao, Z. Yu and N. Li, *J. Mater. Chem. B*, 2016, **4**, 7204–7219.

29 J. Fan, L. Kang, X. Cheng, D. Liu and S. Zhang, *Nanomaterials*, 2022, **12**, 4473.

30 A. C. Pena, L. M. Raymundo, L. F. Trierweiler and M. Gutterres, *J. Ind. Eng. Chem.*, 2023, **117**, 130–139.

31 A. K. Singh, V. K. Singh, M. Singh, P. Singh, S. R. Khadim, U. Singh, B. Koch, S. Hasan and R. Asthana, *J. Photochem. Photobiol., A*, 2019, **376**, 63–72.

32 X. Gong, Y. Liu, Z. Yang, S. Shuang, Z. Zhang and C. Dong, *Anal. Chim. Acta*, 2017, **968**, 85–96.

33 S. Bhatt, M. Bhatt, A. Kumar, G. Vyas, T. Gajaria and P. Paul, *Colloids Surf., B*, 2018, **167**, 126–133.

34 F. Yarur, J.-R. Macairan and R. Naccache, *Environ. Sci.: Nano*, 2019, **6**, 1121–1130.

35 Z. Liu, W. Jin, F. Wang, T. Li, J. Nie, W. Xiao, Q. Zhang and Y. Zhang, *Sens. Actuators, B*, 2019, **296**, 126698.

36 A. B. Leite, C. Saucier, E. C. Lima, G. S. Dos Reis, C. S. Umpierres, B. L. Mello, M. Shirmardi, S. L. Dias and C. H. Sampaio, *Environ. Sci. Pollut. Res.*, 2018, **25**, 7647–7661.

37 S. P. Bangar, K. Dunno, S. B. Dhull, A. K. Siroha, S. Changan, S. Maqsood and A. V. Rusu, *Food Chem.: X*, 2022, 100507.

38 Z. Riahi, A. Khan, J.-W. Rhim, G. H. Shin and J. T. Kim, *Int. J. Biol. Macromol.*, 2024, **258**, 129302.

39 D. Chang, L. Li, L. Shi and Y. Yang, *Analyst*, 2020, **145**, 8030–8037.

40 Q. Chang, W. Xu, N. Li, C. Xue, Y. Wang, Y. Li, H. Wang, J. Yang and S. Hu, *Appl. Catal., B*, 2020, **263**, 118299.

41 Y. Liu, D. Guo, Y. Gao, B. Tong, Y. Li and Y. Zhu, *Appl. Surf. Sci.*, 2021, **552**, 149503.

42 M. Jia, L. Peng, M. Yang, H. Wei, M. Zhang and Y. Wang, *Carbon*, 2021, **182**, 42–50.

43 S. Sharma, A. Umar, S. K. Mehta and S. K. Kansal, *Ceram. Int.*, 2017, **43**, 7011–7019.

44 J. M. Ávila, M. R. Ayala, Y. Kumar, E. Pérez-Tijerina, M. A. Robles and V. Agarwal, *Chem. Eng. J.*, 2022, **446**, 137171.

45 Y. Ma, Y. Chen, J. Liu, Y. Han, S. Ma and X. Chen, *Talanta*, 2018, **185**, 249–257.

46 D. J. Nelson, N. Gowthaman, B. Sinduja and M. Sethuraman, *Talanta Open*, 2025, 100472.

47 S. Babazadeh, R. Bisauriya, M. Carbone, L. Roselli, D. Cecchetti, E. M. Bauer, S. Sennato, P. Prosposito and R. Pizzoferrato, *Sensors*, 2021, **21**, 6353.

48 R. Bisauriya, S. Antonaroli, M. Ardini, F. Angelucci, A. Ricci and R. Pizzoferrato, *Sensors*, 2022, **22**, 2487.

49 R. Pizzoferrato, R. Bisauriya, S. Antonaroli, M. Cabibbo and A. J. Moro, *Sensors*, 2023, **23**, 3029.

50 S. Lu, Z. Li, X. Fu, Z. Xie and M. Zheng, *Dyes Pigm.*, 2021, **187**, 109126.

51 J. Qiu, D. Zeng, Y. Lin, W. Ye, C. Chen, Z. Xu, G. Hu and Y. Liu, *Spectrochim. Acta, Part A*, 2023, **285**, 121913.

52 A. Hemmati, H. Emadi and S. R. Nabavi, *ACS Omega*, 2023, **8**, 20987–20999.

53 H. Xu, W. Zhan, M. Wan, X. Bao, L. Tang and X. Guan, *Ind. Crops Prod.*, 2025, **227**, 120775.

54 B. Wu, X. Shi, W. Han, T. Wang, C. Wang and L. Jiang, *RSC Adv.*, 2018, **8**, 31793–31802.

55 P. Wu, W. Li, Q. Wu, Y. Liu and S. Liu, *RSC Adv.*, 2017, **7**, 44144–44153.

56 Y. Hao, L. Yu, T. Li, L. Chen, X. Han and F. Chai, *Spectrochim. Acta, Part A*, 2023, **285**, 121865.

57 S. Wang, X. Huo, H. Zhao, Y. Dong, Q. Cheng and Y. Li, *Chem. Phys. Impact*, 2022, **5**, 100112.

58 Z. He, J. Shen, J. Zhang, W. Lin and H. Gu, *ACS Sustainable Chem. Eng.*, 2023, **11**, 13126–13141.

59 T. Mandal, R. N. Senapati, A. K. Ghosh, R. E. Masto and V. Singh, *ACS Sustainable Resour. Manage.*, 2025, **2**, 1786–1796.

60 M. He, X. Fu, G. Du, H. Li, P. P. Zhao and X. Liu, *Packag. Technol. Sci.*, 2023, **36**, 465–472.

61 P. Peng, Z. Chen, X. Li, Y. Wu, Y. Xia, A. Duan, D. Wang and Q. Yang, *Sep. Purif. Technol.*, 2022, **291**, 120901.

62 J. Goswami, S. S. Rohman, A. K. Guha, P. Basyach, K. Sonowal, S. P. Borah, L. Saikia and P. Hazarika, *Mater. Chem. Phys.*, 2022, **286**, 126133.

63 H. Ehtesabi, Z. Hallaji, S. Najafi Nobar and Z. Bagheri, *Microchim. Acta*, 2020, **187**, 1–18.

64 T. Li, L. Dai, Y. Huang, S. Pan, Z. Pang and J. Zou, *J. Environ. Chem. Eng.*, 2021, **9**, 105517.

65 World Health Organisation (WHO), in *Water Quality Standards*, 2011, p. 340.

66 Department of Water Affairs and Forestry, South Africa, *South African Water Quality Standard Guidelines, in A.* W. Quality Standard for Cr(VI), 1996, 4, pp. 52–56.

67 L. Zhu, D. Shen and K. H. Luo, *J. Colloid Interface Sci.*, 2022, **617**, 557–567.

68 R. Wang, K.-Q. Lu, Z.-R. Tang and Y.-J. Xu, *J. Mater. Chem. A*, 2017, **5**, 3717–3734.

69 H. Ding, Y. Ji, J.-S. Wei, Q.-Y. Gao, Z.-Y. Zhou and H.-M. Xiong, *J. Mater. Chem. B*, 2017, **5**, 5272–5277.

70 A. K. Garg, J. Kaushik, D. Saini, R. Aggarwal and S. K. Sonkar, *J. Inst. Eng. (India):Ser. E*, 2020, 1–9.

71 H. Zhang, Y. Huang, Z. Hu, C. Tong, Z. Zhang and S. Hu, *Microchim. Acta*, 2017, **184**, 1547–1553.

72 C. Ding, Z. Deng, J. Chen and Y. Jin, *Colloids Surf., B*, 2020, **189**, 110838.

73 A. Tyagi, K. M. Tripathi, N. Singh, S. Choudhary and R. K. Gupta, *RSC Adv.*, 2016, **6**, 72423–72432.

74 S. Wang, H. Zhao, J. Yang, Y. Dong, S. Guo, Q. Cheng, Y. Li and S. Liu, *ACS Omega*, 2023, **8**, 6550–6558.

75 A. A. Castro, A. I. P. Cordoves and P. A. M. Farias, *Anal. Chem. Insights*, 2013, **8**, 21–28.

76 F. Bruno, A. Sciortino, G. Buscarino, M. Cannas, F. M. Gelardi, F. Messina and S. Agnello, *Appl. Sci.*, 2021, **11**, 10360.

77 N. K. R. Bogireddy, S. E. S. Rios and V. Agarwal, *Chem. Eng. J.*, 2021, **414**, 128830.

78 B. Barik, L. Behera and S. Mohapatra, *Ind. Eng. Chem. Res.*, 2023, **62**, 10849–10860.

79 G. Qiao, D. Lu, Y. Tang, J. Gao and Q. Wang, *Dyes Pigm.*, 2019, **163**, 102–110.

80 S. H. Frisbie, E. J. Mitchell and B. Sarkar, *Environ. Health*, 2015, **14**, 63.

81 P. Singh, N. Rani, S. Kumar, P. Kumar, B. Mohan, V. Bhankar, N. Kataria, R. Kumar and K. Kumar, *J. Cleaner Prod.*, 2023, 137474.

82 X. Ma, Y. Dong, H. Sun and N. Chen, *Mater. Today Chem.*, 2017, **5**, 1–10.

83 T.-Y. Shen, P.-Y. Jia, D.-S. Chen and L.-N. Wang, *Spectrochim. Acta, Part A*, 2021, **248**, 119282.

84 A. McEnroe, E. Brunt, N. Mosleh, J. Yu, R. Hailstone and X. Sun, *Talanta Open*, 2023, **7**, 100236.

85 S. D. Torres Landa, I. Kaur and V. Agarwal, *Chemosensors*, 2022, **10**, 532.

86 S. Ding, Y. Gao, B. Ni and X. Yang, *Inorg. Chem. Commun.*, 2021, **130**, 108636.